



# Photooxidation of ethylene glycol and methanol in water solutions over P25 modified with Au, Pt, and Pd

Kseniya Lyzhina <sup>a</sup> , Timur Fazliev <sup>a</sup> , Dmitry Selishchev <sup>a</sup> , Denis Kozlov <sup>a</sup> , Mikhail Lyulyukin <sup>a\*</sup>

<sup>a</sup>: Boreskov Institute of Catalysis SB RAS , Novosibirsk 630090, Russia

\* Corresponding author: [lyulyukin@catalysis.ru](mailto:lyulyukin@catalysis.ru)

## Abstract

One of the actual pollutants of water resources is ethylene glycol, which is part of deicing liquids, high concentrations of which are harmful to humans and nature. This paper describes investigation of the kinetic patterns of photooxidation of ethylene glycol (EG) and methanol (MeOH) as model oxidizable substances on TiO<sub>2</sub> P25 modified with Au, Pt, Pd, under UV irradiation. The study of processes using TOC analysis made it possible to determine the total mineralization of organic substrates, and the analysis of the mixture composition by HPLC, supplemented by modeling the kinetics of oxidation, made it possible to visualize probable transformation routes. Formaldehyde conversion to formic acid showed the lowest surface reaction rate constant in both methanol and ethylene glycol oxidation processes. Acceleration of this step is observed when Pt nanoparticles are applied to the TiO<sub>2</sub> surface. The application of Au has little effect on the rate of decomposition, while the addition of Pd in most cases reduces the observed rates. The study has shown the effect of the metal nature on the course of stepwise ethylene glycol and methanol decomposition and oxidation in aqueous solutions, revealed the ratio between rate constants of these processes, and highlighted the critical need to consider the distribution of the reaction participants between the bulk solution state and the adsorbed one on the surface of the catalyst.

## Key findings

- Oxidation of formaldehyde to formic acid has lowest rate constant for MeOH and EG.
- Stepwise kinetic modeling validated for complex multi-step oxidation pathways.
- Pt boosts all steps; Au and Pd have selective effect; Au promotes C–C bond cleavage in EG.
- Adsorption-based model outperforms traditional pseudo-first-order kinetics.

© 2026, the Authors. This article is published in open access under the terms and conditions of the Creative Commons Attribution (CC BY) license (<http://creativecommons.org/licenses/by/4.0/>), which permits unrestricted re-use of the work in any medium provided the original work is properly cited.

## 1. Introduction

Water contamination by various molecular pollutants poses a critical challenge, as water is a fundamental resource essential for all living organisms to sustain life [1]. Numerous methods exist for removing molecular contaminants from the environment, including filtration, coagulation, flocculation, biological treatment, adsorption/absorption, precipitation, physical and chemical treatment, and membrane systems. However, all these approaches have inherent limitations, restricting their effectiveness in water purifica-

tion. In this context, photocatalysis [2] represents a promising and environmentally benign approach for the elimination of molecular pollutants, especially due to potential utilization of solar energy [3–5] to convert contaminants into minimally hazardous forms, thereby reducing the amount of toxic pollutants in water [6–8]. Nevertheless, water quality continues to deteriorate globally, reaching contamination levels where water may pose risks to both human health and ecosystems.

A prominent example of a water pollutant is ethylene glycol (EG) – a primary component of aircraft deicing fluids

## Accompanying information

### Article history

Received: 13.01.2026

Revised: 16.02.2026

Accepted: 16.02.2026

Available online: 17.02.2026

### Keywords

Pollutant degradation; Photocatalysis; TiO<sub>2</sub>; Methanol (MeOH); Ethylene glycol (EG); Intermediate products

### Funding

The work was supported by the Ministry of Science and Higher Education of the Russian Federation within the framework of the state assignment for the Boreskov Institute of Catalysis, Siberian Branch, Russian Academy of Sciences (project FWUR-2024-0036).

### Supplementary information

Supplementary materials:

Transparent peer review:

### Sustainable Development Goals



and automotive antifreeze/coolants [9–11] and EG concentrations can reach 25–250 g/L in airport wastewater [12,13]. In lake waters located near frequent EG usage sites, concentrations up to 19 g/L have been measured [12]. With a toxicity class 3 rating, ethylene glycol can cause chronic poisoning in humans, adversely affecting vital organs including the blood vessels, kidneys, and nervous system [14]. Furthermore, microorganisms in contaminated water can utilize EG as a carbon source [15,16] – this biological oxidation of EG leads to depletion of dissolved oxygen, adversely affecting larger aquatic life through the development of hypoxia/anoxia and eutrophication [16].

Several methods for EG processing in aqueous solutions have been reported:

- Electrochemical conversion of EG to CO<sub>2</sub> [17,18];
- Photo-Fenton systems [9,10,12];
- EG photooxidation via H<sub>2</sub>O<sub>2</sub> activation using UV-C radiation [15];
- Photocatalytic EG decomposition for H<sub>2</sub> production under anaerobic conditions [19,20].

Studies often evaluate EG degradation via total organic carbon (TOC) or chemical oxygen demand (COD) [21,22] values. However, these analytical methods do not provide a complete picture of intermediate oxidation pathways, limiting the ability to identify rate-limiting steps in complete EG mineralization sequence. Much research focuses not on water purification but on H<sub>2</sub> production, with methanol frequently used as a model electron donor (hole scavenger) in photocatalytic water splitting [23–25]. Similarly, other organic substrates – glycerol [26], isopropanol [27,28], ethanol [26,28], triethanolamine [26], carboxylic acids [26], and biomass components [29] – serve as H<sub>2</sub> sources. Methanol is also employed as a model compound for studying ·OH radical kinetics in TiO<sub>2</sub>-based systems, acting as an ·OH trap [23,30]. A scientific debate persists regarding whether methanol oxidation proceeds via direct hole transfer from the catalyst surface to adsorbed molecules or through ·OH radical attack. Notably, most studies track methanol oxidation only to formaldehyde (often the sole detected product) [24] or neglect further transformation entirely [23].

Thus, literature lacks comprehensive studies on complete oxidative mineralization of organic water pollutants with detailed mechanistic elucidation of intermediate steps. Most reports monitor parent compound disappearance or TOC reduction without mechanistic insights. It should be noted that H<sub>2</sub> production under anaerobic conditions – a fundamentally different process from oxidative degradation. This highlights a critical need for systematic investigations targeting complete photocatalytic mineralization pathways to advance sustainable water purification technologies.

TiO<sub>2</sub>-based photocatalysts are promising for environmental applications, particularly in water purification. Titanium dioxide is the most widely used photocatalyst due

to its low toxicity, high thermal, chemical, and photochemical stability, as well as reasonable cost [31–33]. Under UV irradiation, electrons in TiO<sub>2</sub> are photoexcited from the valence band (VB) to the conduction band (CB), thus generating electron-hole pairs. These charge carriers drive redox reactions that lead to the degradation of pollutants. These reactions follow the primary interfacial charge carrier transfer processes: electrons are captured by an acceptor, while holes are transferred to an electron-donor substrate [34].

In photocatalytic liquid-phase oxidation, dissolved molecular oxygen acts as the electron acceptor, while water or adsorbed organic substrate serves as the electron donor for reaction with photogenerated holes [35,36]. These processes are made possible by the relative energetic positions of TiO<sub>2</sub> valence and conduction bands [37,38]: VB potential (almost similar for anatase and rutile (+2.9 V vs. NHE) is more positive than the water oxidation potential ( $E^\circ(\text{H}_2\text{O}/\cdot\text{OH}) = +2.7 \text{ V vs. NHE}$ ), while CB electron potential (-0.3 V vs. NHE for anatase and -0.1 V vs. NHE for rutile) is more negative than the oxygen reduction potential ( $E^\circ(\text{O}_2/\text{O}_2\cdot^-) = -0.18 \text{ V vs. NHE}$ ). In rutile, CB position hinders superoxide radical (O<sub>2</sub><sup>·-</sup>) formation, but a two-electron reduction pathway yielding hydrogen peroxide ( $E^\circ(\text{O}_2/\text{H}_2\text{O}_2) = +0.695 \text{ V vs. NHE}$ ) remains thermodynamically accessible [39].

The well-known commercial TiO<sub>2</sub> Evonik P25 is a mixture of anatase (~80%) and rutile (~20%) and the formation of a heterojunction between these two phases is responsible for the enhanced photocatalytic activity of P25 relative to pure anatase or rutile alone [40,41]. A significant drawback of pure anatase and rutile, like all individual semiconductors, is the high recombination rate of charge carriers [42]. This effect can be mitigated by modifying the TiO<sub>2</sub> surface with metals, as it facilitates electron transfer from the titanium dioxide conduction band to the impurity levels introduced by the metal [42–44]. This promotes spatial charge separation and suppresses their recombination. For TiO<sub>2</sub> surface modification with metallic nanoparticles (metals readily reduced to their metallic state, such as Pt, Pd, and Au) are commonly used. In photocatalysis, Pt-modified TiO<sub>2</sub>-based catalysts are most widespread because platinum deposition significantly enhances reaction rates in both gas-phase [45] and liquid-phase systems [31]. This enhancement in activity is attributed not only to improved charge separation but also to the role of Pt as a cocatalyst in surface transformations [46]. The higher activity of Pt/TiO<sub>2</sub> compared to Ag/TiO<sub>2</sub> [31] is linked both to the higher work function of Pt and to its lower overpotential for H<sub>2</sub> generation. Pure TiO<sub>2</sub> and other wide-bandgap semiconductors typically exhibit high overpotential value [47].

Different metals exhibit varying abilities to catalyze the proposed rate-limiting hydrogen evolution step [48]. The rates of formaldehyde formation from ethylene glycol and hydrogen evolution decreased in the order Pt > Au ≈ Pd >>

pristine TiO<sub>2</sub>. Although the work functions of Pt and Pd are close (5.3 eV, 5.7 eV, and 5.6 eV for Au (111), Pt (111), and Pd (111), respectively [49]), their activities differ, indicating the contribution of multiple factors. Comparing Pt and Pd is interesting, because thermal catalytic processes achievable with these metals [50,51] could affect photocatalytic performance. Furthermore, it was shown [39] that Pd-modified rutile exhibits pronounced photoactivity in hydrogen peroxide generation, suggesting that the metal also affects the formation and/or accumulation of reactive oxygen species. Au is another metal frequently used for TiO<sub>2</sub> modification. Despite the outer electron shells of Pt and Au differing by just one electron, their properties are markedly different. Therefore, depositing these metals will have distinct effects on the final photoactivity of the sample [48]. Conversely, a study on the photodegradation of the dye acid green 16 [43] reported that the quantum efficiency of Pt/TiO<sub>2</sub> was comparable to that of Au/TiO<sub>2</sub> but superior to Pd/TiO<sub>2</sub>. Thus, it is meaningful to compare photocatalysts modified with different metals (Pt, Pd, Au), as the metal on the TiO<sub>2</sub> surface not only acts as an electron acceptor for efficient charge separation (as traditionally understood in photocatalysis) but also participates in activating intermediate steps and interacts with reactive oxygen species.

So, P25 was chosen as the benchmark photocatalyst for two key reasons, which directly define its interaction with deposited metals (Au, Pt, Pd): the intrinsic anatase/rutile heterojunction and Schottky junction with the metal cocatalyst. The former provides superior intrinsic charge separation, ensuring that any observed enhancement originates primarily from interaction of metal with titania, rather than from improved semiconductor. The latter promotes the transfer of photogenerated electrons to metal nanoparticles, leading to effective charge separation, activation of metals as cocatalysts for multi-electron reactions (e.g., O<sub>2</sub> reduction), and influence on degradation pathway kinetics. Therefore, P25 allows isolation of the synergistic effect between semiconductors and different noble metal cocatalysts during pollutant oxidation.

The aim of this work was to investigate the photocatalytic oxidation of ethylene glycol and methanol in aqueous solutions in the presence of titanium oxide catalysts under UV irradiation, with a detailed analysis of the model compound decomposition kinetics and the dynamics of formation and consumption of water-soluble intermediate degradation products. The catalysts examined include the well-known commercially available P25, as well as P25 modified with deposited Pt, Pd, and Au. The experimental data obtained were used to develop a kinetic transformation model, which enabled the calculation of apparent rate constants for the corresponding process steps through numerical simulation and demonstrated their dependence on the nature of the metal used to modify P25. The findings are significant for understanding the key steps in the degradation of such compounds and for developing strategies

to enhance the decomposition of aqueous contaminants.

## 2. Materials and methods

### 2.1. Chemicals

Ethylene glycol (C<sub>2</sub>H<sub>6</sub>O<sub>2</sub>, Reachim, Russia), methanol (CH<sub>3</sub>OH, 99.8%, J.T. Baker, Netherlands), formaldehyde (CH<sub>2</sub>O) and formic acid (CH<sub>2</sub>O<sub>2</sub>) standard solutions were purchased from Reachim, Russia, glycolaldehyde dimer (C<sub>4</sub>H<sub>8</sub>O<sub>4</sub>, 98%, Fluka Chemie, Switzerland), glycolic acid (C<sub>2</sub>H<sub>4</sub>O<sub>3</sub>, 98%, BLD Pharmatech, USA), oxygen (99.9%), AEROXIDE TiO<sub>2</sub> Evonik P25 (Evonik Industries, Germany), metal precursors including hydrogen hexachloroplatinate (H<sub>2</sub>PtCl<sub>6</sub>), palladium chloride (PdCl<sub>2</sub>), hydrogen tetrachloroaurate (HAuCl<sub>4</sub>) were purchased from Krastsvetmet JSC, Russia, sodium tetrahydridoborate (NaBH<sub>4</sub>, 98%, Acros Organics, Belgium).

### 2.2. Synthesis of Me-modified photocatalysts

The synthesis of metal-modified TiO<sub>2</sub> photocatalysts was carried out using a reductive deposition method [52] with sodium borohydride (NaBH<sub>4</sub>), following the procedure below. A 0.5 g sample of TiO<sub>2</sub> Evonik P25 was dispersed in 50 ml of deionized water and stirred for 10 minutes. Under continuous stirring, a solution of the metal precursor (0.5% metal by mass) was added to the suspension, followed by 30 min of mixing. A freshly prepared NaBH<sub>4</sub> solution was then added dropwise at a molar ratio of metal to NaBH<sub>4</sub> of 1:3. After 3 h of stirring, the resulting precipitate was washed five times with deionized water via centrifugation (11000 g, 30 min, Beckman Coulter, USA).

### 2.3. Characterization of catalysts used

Diffuse reflectance spectra (DRS) for the samples were recorded in the 250–850 nm range (1 nm step) using a Cary 300 UV-Vis spectrophotometer (Agilent, USA) equipped with a DRA-30I integrating sphere attachment. Polytetrafluoroethylene (PTFE) from Agilent (USA) was used as the reference material. The spectra were converted using the Kubelka-Munk function  $F(R)$

$$F(R) = \frac{(1-R)^2}{2R}, \quad (1)$$

where  $R$  – reflectance (%), to construct Tauc plots, which represent the dependence of  $(F(R) \cdot hv)^{0.5}$  on the photon energy  $hv$ . Analysis of the DRS data via Tauc plot transformation enables estimation of the semiconductor optical band gap energy, determined as the value on the abscissa axis at the intersection point of the baseline and the extrapolated linear fit [53,54].

The phase composition of the synthesized samples was confirmed by X-ray diffraction (XRD) analysis using a Bruker D8 Advance (Germany) X-ray diffractometer with CuK $\alpha$  radiation. The oxidation states of the metals depos-

ited on the TiO<sub>2</sub> surface were determined by X-ray photoelectron spectroscopy (XPS) on a SPECS photoelectron spectrometer (SPECS Surface Nano Analysis GmbH, Germany) equipped with a PHOIBOS-150 hemispherical electron energy analyzer and an AlK $\alpha$  X-ray source (1486.6 eV, 100 W). The specific surface area of the obtained samples was determined by low-temperature (77 K) nitrogen adsorption-desorption using an ASAP 2400 analyzer (Micromeritics, USA). The samples were subjected to vacuum degassing prior to the measurements at 150 °C for 16–24 h.

## 2.4. Photocatalytic experiments

Photocatalytic reactions were carried out in a thermostatic glass reactor at 25 °C. 85 mg of photocatalyst was suspended in 170 mL of an aqueous solution of organic compound – methanol or ethylene glycol (typically 500 mg L<sup>-1</sup>). Deionized water (Barnstead EasyPure II, 18.2 M $\Omega$  cm) was used to prepare model solutions. The reaction slurry was saturated with dissolved oxygen by O<sub>2</sub> bubbling at a flow rate of 20 mL min<sup>-1</sup>. The reactor was magnetically stirred. Prior to each experiment, the reaction mixture was stirred under dark conditions for 15 min to achieve the adsorption-desorption equilibrium. The reactor was then irradiated using a LED source of UV radiation, with maximum radiation wavelength at 370 nm and radiation intensity of 30 mW cm<sup>-2</sup>. Liquid samples were regularly taken from the reaction slurry through a stainless-steel needle and then filtered through a 0.2  $\mu$ m PTFE HP syringe filter.

Samples were analyzed with Multi N/C 3100 duo TOC/TNb Analyzer (Analytik Jena, Germany) to quantify a Total Organic Carbon (TOC). Before analysis, each sample was acidified with ~50  $\mu$ L of 2 M HCl to remove dissolved CO<sub>2</sub>. Qualitative and quantitative determination of methanol and ethylene glycol oxidation products was carried out using Waters Acquity Arc high-performance liquid chromatograph (HPLC, USA) equipped with a four-channel high-pressure liquid pump, an autosampler, a column thermostat, a refractive index (RI) and photodiode array (PDA) detectors. Separation was performed using a Repromer H 4.6 $\times$ 250 mm ion exclusion column (Dr. Maisch HPLC GmbH, Germany), filled with polymer sorbent granules of 9  $\mu$ m and equipped with a pre-column with the same sorbent. The temperature of the cell of the refractometer and the column thermostat was 50 °C, the temperature of the automatic sampler was 25 °C. A 5 mM solution of sulfuric acid in deionized water was used as the eluent, the flow rate of the eluent 0.5 mL min<sup>-1</sup>, the sample volume 0.010 mL.

## 2.5. Experimental data processing and kinetic modeling

As formaldehyde and formic acid do not achieve separation under the given conditions, and the photodiode detector provides an analytical signal exclusively for formic acid, the concentrations of these components were established via a system of equations for formaldehyde C<sub>FD</sub> (2) and formic

acid C<sub>FA</sub> (3), utilizing known analytical signal areas and pre-determined calibration coefficients.

$$C_{FD} = \frac{A_{RI} - K_{FA}^{RI} C_{FA}}{K_{FD}^{RI}}, \quad (2)$$

$$C_{FA} = \frac{A_{PDA}}{K_{FA}^{PDA}}, \quad (3)$$

where A<sub>RI</sub> and A<sub>PDA</sub> are the analytical signal areas in the RI and PDA channels, respectively; K<sub>FD</sub><sup>RI</sup> is the calibration coefficient for formaldehyde in RI, and K<sub>FA</sub><sup>RI</sup> and K<sub>FA</sub><sup>PDA</sup> are the calibration coefficients for formic acid in RI and PDA, respectively.

Glycolaldehyde (GD) and glycolic acid (GA) also remain unresolved under these chromatographic conditions, but they possess different sensitivity coefficients in RI and PDA. Concentrations of GD and GA were similarly derived from the system of equations (4, 5). Raw chromatographic data examples (Figure S1), component retention times (Table S1), and sensitivity coefficients (Table S2) are presented in Supplementary materials.

$$C_{GD} = \frac{A_{RI} K_{GA}^{PDA} - A_{PDA} K_{GA}^{RI}}{K_{GD}^{RI} K_{GA}^{PDA} - K_{GA}^{RI} K_{GD}^{PDA}}, \quad (4)$$

$$C_{GA} = \frac{A_{RI} - K_{GD}^{RI} C_{GD}}{K_{GA}^{RI}}. \quad (5)$$

The maximum observed rate of the model organic compound mineralization ( $\mu$ mol(C) L<sup>-1</sup> min<sup>-1</sup>) was determined from the dependence of the TOC concentration in the solution on the irradiation time by applying linear approximation to the TOC decay region. The obtained values were used to evaluate the overall mineralization rate of the model pollutant.

The kinetics of the photo-oxidation process were simulated using the Mathcad software package. During the modeling of the oxidation processes, two kinetic models were investigated.

### 2.5.1. First Kinetic Model – Pseudo-First-Order Kinetics

The first model is the widely used pseudo-first-order kinetic model [55–57], which describes the chemical transformation of organic substrates without accounting for process heterogeneity (i.e., ignoring adsorption) or reactor parameters. Calculations were performed using numerical integration followed by solving a system of vector equations, where the variables are the rate constants  $k_j'$  for each transformation step [58]. The general form of the vector equation is given by expression (6), where  $\phi_j(t)$  is the numerically calculated integral (7), and  $C_i(t)$  is the set of experimental data points representing the concentration of  $i^{\text{th}}$  component at time moment  $t$ .

$$C_i(t) = C_{i,0} + \sum_j \nu_{ij} \cdot k_j' \cdot \phi_j(t), \quad (6)$$

where  $\nu_{ij}$  is the stoichiometric coefficient of  $i^{\text{th}}$  component on the stage  $j$ ,  $k_j'$  is the (effective) rate constant of step  $j$ , and  $C_{i,0}$  is the initial concentration of the  $i^{\text{th}}$  component.

$$\varphi_j(t) = \int_0^t \prod_i C_i(t)^{n_{ij}} dt, \quad (7)$$

where  $n_{ij}$  is the reaction order of  $i^{th}$  component on the step  $j$ . As an example, the system of vector equations for methanol transformation (8–11) is provided:

$$C_{MeOH}(t) = C_{MeOH,0} - k_1^{\square} \cdot \int_0^t C_{MeOH}(t) dt, \quad (8)$$

$$C_{FD}(t) = C_{FD,0} + k_1^{\square} \cdot \int_0^t C_{MeOH}(t) dt - k_2^{\square} \cdot \int_0^t C_{FD}(t) dt, \quad (9)$$

$$C_{FA}(t) = C_{FA,0} + k_2^{\square} \cdot \int_0^t C_{FD}(t) dt - k_3^{\square} \cdot \int_0^t C_{FA}(t) dt, \quad (10)$$

$$C_{CO_2}(t) = C_{CO_2,0} + k_3^{\square} \cdot \int_0^t C_{FA}(t) dt. \quad (11)$$

Here and throughout the text, the following notations are used: MeOH – methanol, FD – formaldehyde, FA – formic acid. Furthermore, the model assumes complete oxidation of formic acid to carbon dioxide. The validity of this assumption is supported by findings such as those reported by Nomikos et al. [59], who observed only CO<sub>2</sub> and H<sub>2</sub> in the gas phase during methanol oxidation. Furthermore, in a study [19] on the oxidation of ethylene glycol using Pt/P25, CO was not detected in the gaseous products while CO<sub>2</sub> was. To ensure uniformity across our calculations, we adopted the assumption that oxidation proceeds to completion with each catalyst regardless of the modifying agent. Using the calculated rate constants, the direct kinetic problem was solved by numerical integration of a system of differential equations of the form (12) for current reaction participant concentrations, yielding calculated kinetic curves subsequently compared with experimental data:

$$\frac{dC_{MeOH}(t)}{dt} = -k_1^{\square} C_{MeOH}. \quad (12)$$

### 2.5.2. Second Model – Adsorption-Based Kinetics

The second model accounts for the adsorption of substances on the surface of catalyst samples. It incorporates the number of available adsorption sites on the catalyst and the reactor volume. Thus, the second model (hereafter is referred to as the “adsorption-based model”) considers the total distribution of  $i^{th}$  component in the bulk aqueous solution  $N_{i,aq}$  and on the catalyst surface  $N_{i,s}$  (13):

$$N_i = N_{i,s} + N_{i,aq} = \theta_i N_{\theta} + C_i V, \quad (13)$$

$$\frac{dN_i}{dt} = \sum_j v_{ij} k_j^* \theta_i \theta_{O_2}, \quad (14)$$

where  $\theta_i$  is the surface coverage fraction of  $i^{th}$  component,  $N_{\theta}$  is the maximum number of adsorption sites available for  $i^{th}$  component (monolayer capacity, assumed as  $10^{14}$  cm<sup>-2</sup> [60], the sensitivity of the calculations performed to changes in this value is illustrated in the Supplementary materials),  $V$  is the reaction mixture volume,  $k_j^*$  is the rate constant of step  $j$ , and  $\theta_{O_2}$  is the surface coverage fraction of oxygen molecules, which act as an (indirect) oxidizer in each step. The change in the total amount of the  $i^{th}$  component results from the reaction on the catalyst surface (14).

The observed change in  $i^{th}$  component amount is expressed as (15) and the surface coverage fraction  $\theta_i$  is described by the Langmuir competitive adsorption equation, assuming only carbon-containing transformation participants occupy the surface, while oxygen adsorption is negligible. For instance, in the methanol photooxidation system,  $\theta_i$  takes the form (16):

$$\frac{dC_i}{dt} = \frac{1}{V} \frac{d}{dt} (N_i - \theta_i N_{\theta}) = \frac{1}{V} \sum_j v_{ij} k_j^* \theta_i \theta_{O_2} - \frac{N_{\theta}}{V} \frac{d\theta_i}{dt}, \quad (15)$$

$$\theta_i = \frac{K_i C_i}{1 + K_{MeOH} C_{MeOH} + K_{FD} C_{FD} + K_{FA} C_{FA}}. \quad (16)$$

For calculations using the second model (“adsorption-based model”), a system of differential equations for current concentrations of transformation participants is constructed with initial conditions ( $C_{i,0}$ ) and initial approximations for apparent rate constants (or adsorption equilibrium constants). These are used to solve the direct problem of chemical kinetics. Optimization of rate constants (or adsorption equilibrium constants) is performed by formulating a system of vector equations that equate calculated and experimental values at specific time points  $t_e$ . Optimization minimizes the residual (17), determining constants that maximize agreement between calculated kinetic curves and experimental data [58]. The constants obtained can be used as initial approximations iteratively until the sum of squared deviations ( $SS_{res}$ ) stabilizes.

$$SS_{res} = \sum_{i=1}^N (y_i - \hat{y}_i)^2, \quad (17)$$

where  $y_i$  are actual concentration values and  $\hat{y}_i$  are calculated concentration values at corresponding time points. Below, the differential equation for methanol transformation (18) derived from (15) is provided as an example:

$$\frac{dC_{MeOH}}{dt} = \frac{\frac{1}{V(1+K_{MeOH}C_{MeOH}+K_{FD}C_{FD}+K_{FA}C_{FA})^2} \cdot k_1 K_{MeOH} C_{MeOH}}{1 + \frac{N_{\theta}}{V(1+K_{MeOH}C_{MeOH}+K_{FD}C_{FD}+K_{FA}C_{FA})}}, \quad (18)$$

where  $k_1$  is the rate constant for MeOH-to-FD conversion, defined by (19):

$$k_j = k_j^* \cdot K_{O_2} \cdot C_{O_2}. \quad (19)$$

Since O<sub>2</sub> bubbling maintains a stable O<sub>2</sub> concentration in the reaction mixture, the product of the rate constant  $k_j^*$ , adsorption equilibrium constant, and oxygen concentration is treated as constant.

### 2.5.3. Accuracy Evaluation

The adjusted coefficient of determination  $R^2_{cor}$  was used to evaluate the accuracy of the calculated kinetic curves [61,62] against experimental data (20)–(23). The total sum of squares is defined as (20):

$$SS_{tot} = \sum_{i=1}^N (y_i - \bar{y})^2, \quad (20)$$

where  $\bar{y}$  is the mean value of experimental concentration values (21):

$$\bar{y} = \frac{1}{N} \sum_{i=1}^N y_i. \quad (21)$$

The coefficient of determination  $R^2$  is defined by (22) and used to calculate  $R^2_{cor}$  (23).

$$R^2 = 1 - \frac{SS_{res}}{SS_{tot}}, \quad (22)$$

$$R^2_{cor} = 1 - (1 - R^2) \frac{(n-1)}{(n-k)}, \quad (23)$$

where  $n$  is the number of experimental points and,  $k$  is the number of variables.

### 3. Results and discussion

#### 3.1. Photocatalysts characteristics

The diffuse reflectance spectra for the 0.5% M/P25 samples (where M = Pt, Pd, Au), prepared via sodium borohydride-assisted reductive deposition, are presented in Figure 1. For comparison, the diffuse reflectance spectrum of the pristine P25 is also provided. Additionally, the corresponding Tauc plots for the 0.5% M/P25 samples are provided. Analysis of the diffuse reflectance spectra via Tauc plot transformation allows for the calculation of the optical band gap energy of the semiconductor, enabling determination of the values for both the anatase and rutile phases present in the commercial TiO<sub>2</sub> P25 material.

It should be noted that this type of analysis provides estimated band gap values. Consequently, depending on the sample preparation method, the calculated values can vary slightly (by approximately 0.1 eV for both rutile and ana-

tase), while no actual change in  $E_g$  occurs. Measured specific surface area of the mentioned samples showed almost no deviation from the initial value of 56 m<sup>2</sup> g<sup>-1</sup> measured for the pristine P25 because of mild synthesis conditions. All 0.5% M/P25 samples exhibit absorption in the visible region due to absorption by the metal nanoparticles. In the near-UV region, absorption for the 0.5% M/P25 samples remains attributable to the intrinsic absorption of P25, indicating that the semiconductor's structure remains unaltered by the surface metal deposition. The XRD analysis revealed that no diffraction peaks corresponding to crystalline phases other than the original titania phases of TiO<sub>2</sub> P25 material were detected in the samples with a 0.5% metal loading. Furthermore, the data confirms that the anatase-to-rutile phase ratio remains unchanged also (Figure S3 and Table S3).

According to XPS data (Figure 2), the atoms in the Pt nanoparticles are entirely in the metallic state, while Pd is partially in the Pd<sup>2+</sup> state (about 30%), which is quite common for Pd-based TiO<sub>2</sub> systems [39,63], and Au is partially in Au<sup>+</sup> state (about 15%) being usually observed for Au nanoparticles [64,65]. Our conclusions regarding the presence of metal nanoparticles on the surface are based on electron microscopy data (SEM and TEM). It should be noted that at a low metal mass loading, nanoparticles may not be uniformly distributed or visible in every field of view. However, the micrographs capture characteristic nanoscale features that we attribute to metal particles (Figure S5).

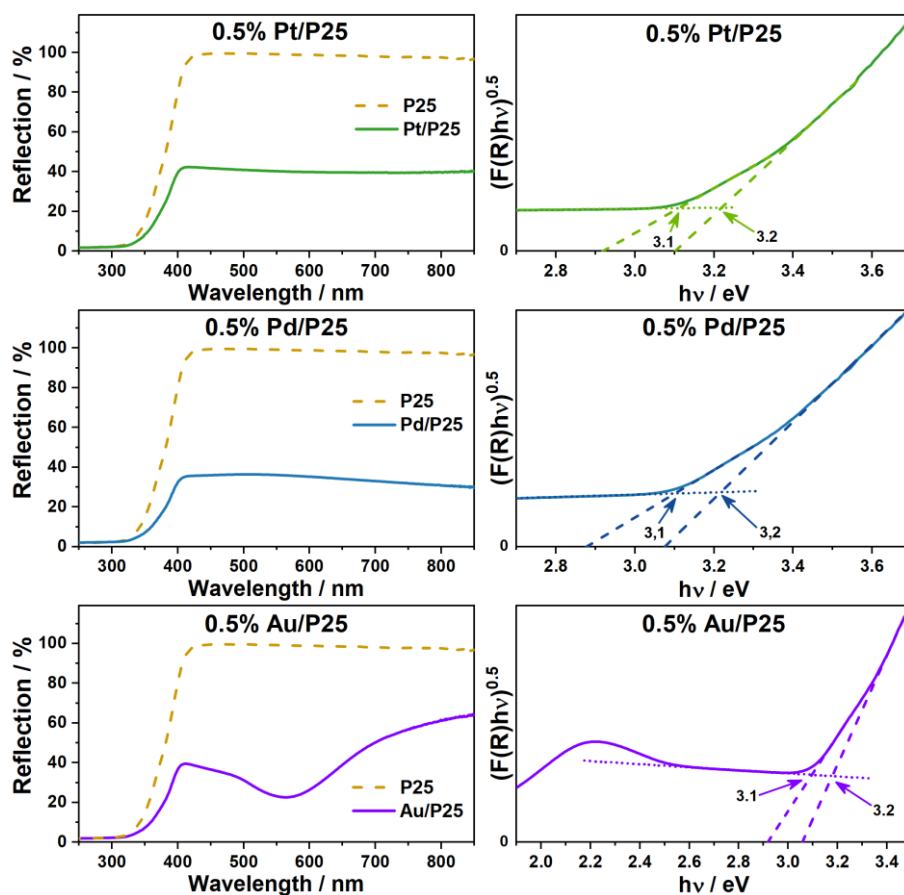


Figure 1 Absorption spectra of pure P25 and synthesized samples and determination of the bandgap by the Tauc method.

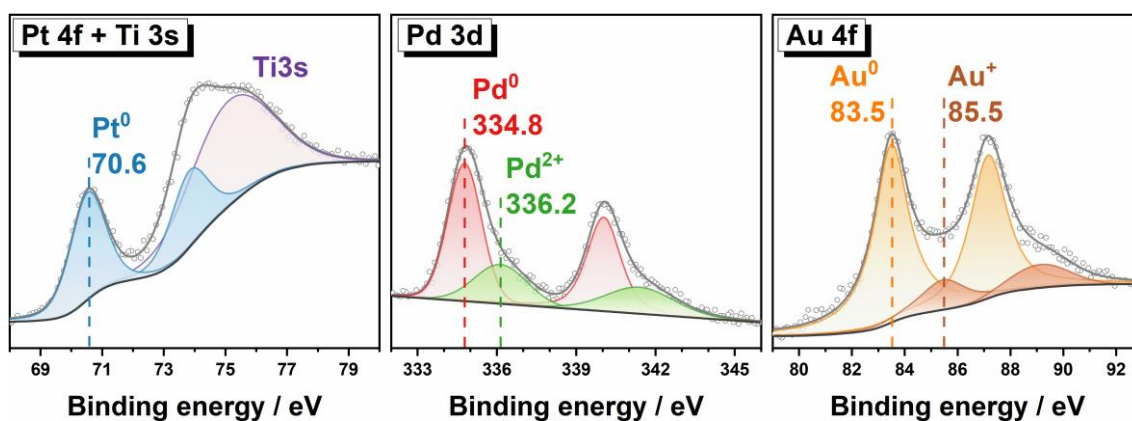


Figure 2 XPS data for synthesized samples.

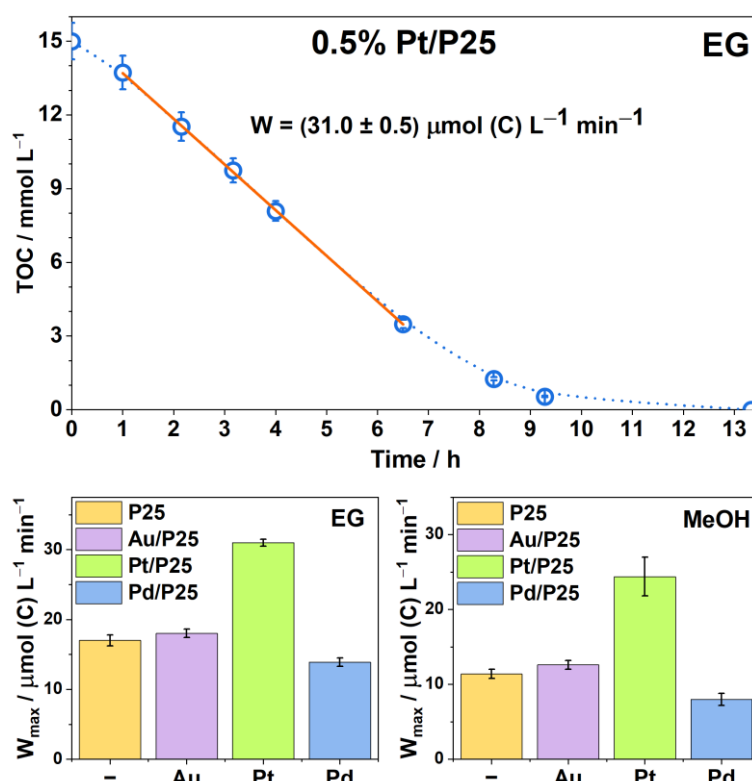


Figure 3 TOC data for EG photocatalytic oxidation over 0.5% Pt/P25 sample; EG and MeOH mineralization rates.

### 3.2. Ethylene glycol and methanol mineralization over Me-modified P25

Based on the TOC measurement (Figure 3), the maximum rates of ethylene glycol (EG) and methanol (MeOH) mineralization were calculated for the synthesized 0.5% M/P25 samples. Although ethylene glycol has a more complex molecular structure than methanol, its photocatalytic oxidation rate is somewhat higher. This may be attributed to adsorption features to be shown later.

Metal particles on the titania surface are known to serve as acceptors for photogenerated electrons from the conduction band of semiconductors by overcoming the Schottky barrier. This promotes charge separation and inhibits recombination. In both cases, for ethylene glycol and methanol, the deposition of metals alters the activity of P25 in such way:

- most rapid oxidation up to CO<sub>2</sub> occurs in the presence of the Pt-modified P25;
- addition of Au onto P25 surface causes minimal changes to the mineralization rate;
- addition of Pd reduces the mineralization rate.

These differences may be attributed to distinct metal characteristics, such as work function and electron affinity. Variations in reaction mechanisms and the energy of generated reactive oxygen species (ROS) could also contribute. Furthermore, metal cocatalysts can initiate parallel side reactions that influence the efficiency of the studied processes. For instance, previous results show that Pd<sup>2+</sup> species supported on the anatase phase accelerate the hydrogen peroxide decomposition [39], which may explain the observed decline in mineralization rate.

A detailed analysis of the TOC decay kinetics reveals a nonlinear pattern: an initial induction period is observed,

followed by accelerated linear TOC depletion, which subsequently decelerates as values tend to zero. This behavior is associated with the formation and decomposition of intermediate organic oxidation products. A thorough investigation of these kinetics has become the focus of further research.

### 3.3. Methanol oxidation pathway research and kinetic modelling

Analysis of oxidation intermediates revealed that methanol oxidation proceeds via a stepwise mechanism, involving sequential formation of formaldehyde and formic acid, with subsequent conversion to gaseous products (Figure 4). Hereafter, gaseous products are denoted as  $\text{CO}_x$  in the proposed reaction schemes to ensure greater accuracy because, for instance, in the study [20] both  $\text{CO}_2$  and  $\text{CO}$  were detected among ethylene glycol oxidation products. The reaction pathway remains consistent across different catalyst compositions; however, the rates of intermediate steps vary significantly.

A notable accumulation of formaldehyde was observed in the reaction mixture, likely attributed to its weak adsorption on the catalyst surface [19]. Consequently, while methanol concentration remains high, formaldehyde consumption is limited due to competitive adsorption for active sites. In contrast, the concentration of formic acid reaches a pseudo-stationary level and remains nearly constant over an extended period.

#### 3.3.1. Pseudo-first order kinetic model

The application of the pseudo-first-order kinetic model to describe methanol oxidation shows satisfactory results (Figure 5). However, a noticeable discrepancy between the model and experimental data is observed, as this model

does not account for the competitive adsorption of reaction participants on the catalyst surface.

Using the pseudo-first-order model, the rate constant  $k_j'$  for each stage of methanol conversion was calculated for the 0.5% M/P25 catalysts (Figure 5). These  $k_j'$  values are not true rate constants but represent apparent rate constants obtained under the assumption that each step follows first-order kinetics.

For all samples, the highest value corresponds to the formic acid conversion rate constant  $k_3'$ . The conversion processes of methanol and formaldehyde proceed at a lower rate. The rate constant for FD-to-FA conversion  $k_2'$  increases with Pt modification, while Au and Pd deposition do not significantly accelerate this step. According to the pseudo-first-order model calculations, the initial methanol oxidation step is rate-limiting. Notably, modification of  $\text{TiO}_2$  P25 does not significantly increase  $k_1'$ , neither for 0.5% Pt/P25 nor for both other catalysts.

It should be noted that the high efficiency of Pt/P25 arises from a synergistic effect between its direct chemical participation and catalytic activity in the transformation of intermediates even without irradiation (Figure S14) and its indirect role in enhancing the photocatalytic process through improved charge separation [66,67]. Deconvoluting the contribution of each factor was not a distinct aim of this work. Nevertheless, the kinetic data indicates a specific action of Pt that extends beyond merely increasing the charge carrier's concentration.

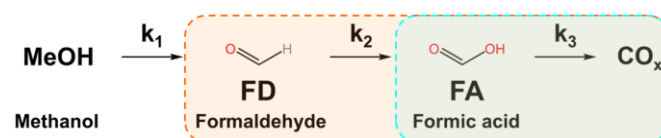


Figure 4 Proposed scheme for methanol oxidation, including main water-dissolved intermediates: formaldehyde and formic acid.

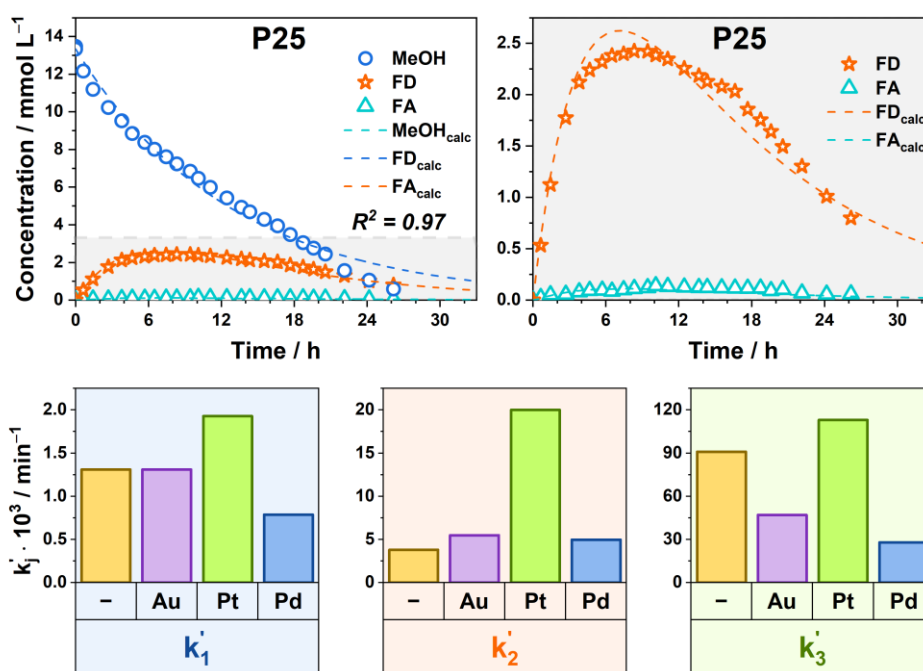


Figure 5 Pseudo-first order kinetic model application for MeOH oxidation. Calculated rate constants for main oxidation steps.

### 3.3.2. Kinetic model enhancement

Given the insufficient accuracy of the initial model in describing the experimental data, we refined it by accounting for the distribution of reaction components between the solution bulk and the catalyst surface. Due to the system's complexity – involving at least three rate constants and, when adsorption is considered, three additional adsorption equilibrium constants – the methanol oxidation process was studied stepwise. This approach reduces the number of independent variables in calculations. Following the methodology described in Section 2.4, experiments on the photocatalytic oxidation of formic acid and formaldehyde were conducted. The results gave the rate constant for FA-to-CO<sub>2</sub> ( $k_3$ ) and FD-to-FA ( $k_2$ ) oxidation, which were subsequently used for complex systems. The following section focuses on refining the first model using FA oxidation as an example and applying the enhanced adsorption-based model to FD oxidation.

Figure 6 shows the concentration profile of formic acid (FA) during its oxidation on P25. Figure shows that the pseudo-first-order model based on equation (24) fails to describe adequately the experimental data.

$$\frac{dC_{FA}}{dt} = -k_3 \cdot C_{FA} \quad (24)$$

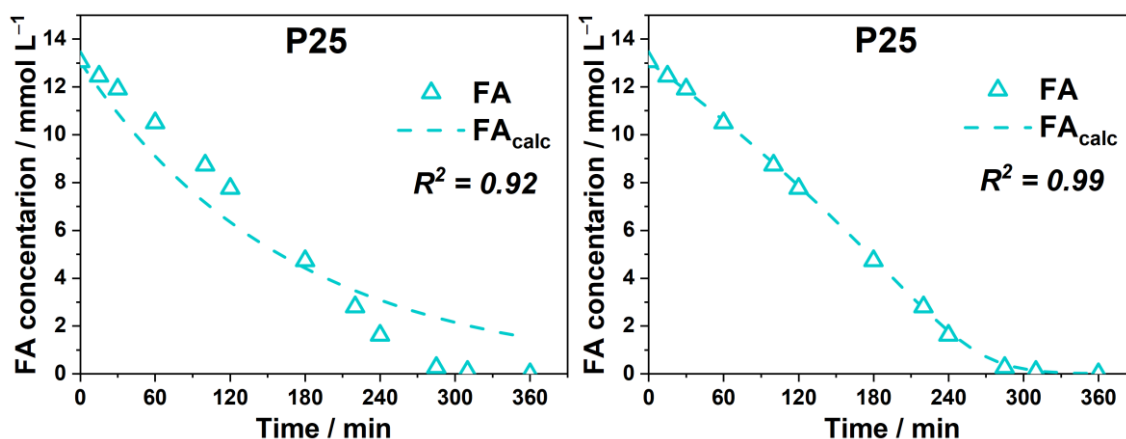


Figure 6 Formic acid oxidation data described with pseudo-first-order kinetic model (left) and adsorption-based model (right).

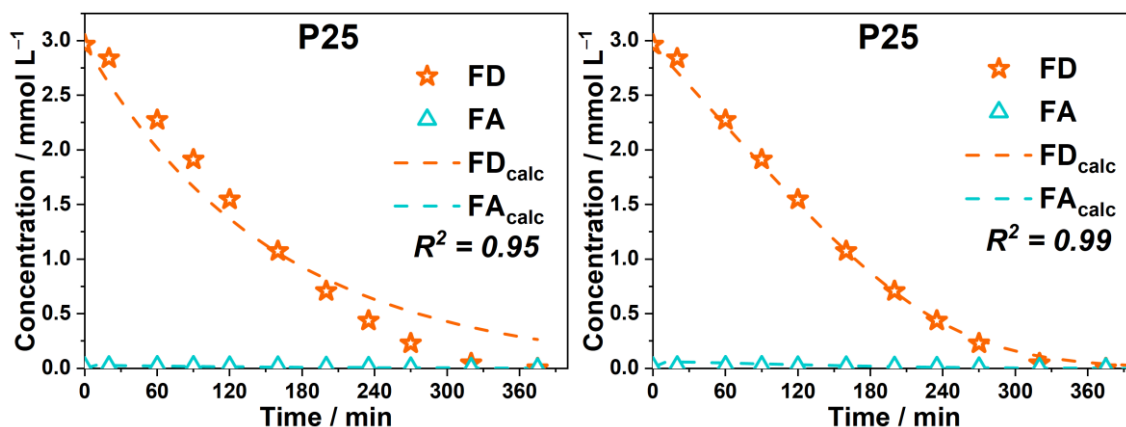


Figure 7 Formaldehyde oxidation data described with pseudo-first-order kinetic model (left), adsorption-based model (right).

The adsorption-based model, which accounts for the distribution of components between the bulk liquid phase and the catalyst surface, demonstrates better agreement with the experimental data ( $R^2 = 0.99$ ). Within this model, the change in FA concentration is expressed as follows (25):

$$\frac{dC_{FA}}{dt} = \frac{\frac{1}{V} \frac{k_3 K_{FA} C_{FA}}{(1+K_{FA} C_{FA})^2}}{1 + \frac{K_{FA}}{V(1+K_{FA} C_{FA})^2}}, \quad (25)$$

where  $k_3$  is the rate constant for FA oxidation to CO<sub>2</sub>, and  $K_{FA}$  is the adsorption equilibrium constant of FA.

Using the example of formic acid oxidation, the Langmuir-Hinshelwood model is also shown, which, like the pseudo-first-order model, is often used in modeling photocatalytic oxidation processes. The results obtained are presented in Figure S2.

Similarly to formic acid, the accuracy of describing formaldehyde (FD) oxidation kinetics can be demonstrated using both models: Figure 7 shows the application of both models for formaldehyde oxidation evaluation. For the calculations using the adsorption-based model, the formic acid oxidation rate constants  $k_3$  obtained in the previous stage (Figure 6) were used.

### 3.3.3. Adsorption-based model application for methanol photooxidation

The rate constants for FD-to-FA ( $k_2$ ) and FA oxidation ( $k_3$ ) obtained via the adsorption-based model implementation were applied to methanol oxidation process. Figure 8 presents the results of MeOH oxidation kinetics, accounting for the distribution of components between the reactor volume and the catalyst surface. The application of the adsorption-based model enables an accurate description of MeOH oxidation kinetics ( $R^2 = 0.99$ ). Unlike the pseudo-first-order model, which describes MeOH decay as exponential (Figure 5), the adsorption-based model captures the initial rapid MeOH decrease followed by gradual slowdown. This deceleration is surely attributed to intermediate products accumulating on the catalyst surface, especially formaldehyde.

In all cases, the highest rate constant is that for FA oxidation ( $k_3$ ), indicating this step as the fastest. According to these results, the lowest calculated reaction rate constant is the FD-to-FA oxidation ( $k_2$ ). In contrast, applying the pseudo-first-order model yields a conclusion that the lowest value is  $k_1'$ , suggesting the MeOH-to-FD process step is the slowest. Indeed, this discrepancy does not represent a contradiction between the two models: as  $k_1'$  in the first case is an apparent constant, its expression incorporates at least the true rate constant and the adsorption equilibrium constant for methanol. Thus, while the FD-to-FA oxidation has the lowest reaction rate constant, the MeOH-to-FD conversion step limits the overall reaction rate.

### 3.3.4. Adsorption issues

When discussing component distribution on the catalyst surface within the adsorption-based model framework, surface coverage by reaction participants should be considered

with the adsorption-desorption equilibrium constants. It is important to note that this equilibrium can be disrupted during the reaction due to the high rate of component consumption or formation [55,68]. Consequently, the expression for the apparent adsorption equilibrium constant takes the form:

$$K = \frac{k_{\text{ads}} + k_{\text{form}}}{k_{\text{des}} + k_{\text{deg}}}, \quad (26)$$

where  $k_{\text{ads}}$  is the adsorption rate constant,  $k_{\text{des}}$  is the desorption rate constant,  $k_{\text{form}}$  is the formation rate constant and  $k_{\text{deg}}$  is the degradation rate constant for reaction component considered. Furthermore, the adsorption-desorption equilibrium is disrupted by the formation of charged reactive species on the catalyst surface. This directly affects, for example, the adsorption of acids capable of dissociation. As a result, using adsorption equilibrium constants determined experimentally under static conditions does not lead to a reasonable description of the kinetic data. The same way the values of equilibrium constants obtained through parameter optimization in calculations are distorted due to the disruption of adsorption equilibrium and do not match the experimental values. Therefore, for each specific system to be modeled, unique equilibrium constants will be obtained for all reaction participants. For instance, in the  $\text{FA} \rightarrow \text{CO}_2$  and  $\text{FD} \rightarrow \text{FA} \rightarrow \text{CO}_2$  transformation chains, the adsorption equilibrium constants for FA will not be identical. In the first case, the value of  $K_{\text{FA}}$  will be influenced by the FA consumption rate, while in the second one, it will also be affected by the FA formation rate. If the calculated rate constants remain same from system to system (being true constants independent of substance concentration and the presence of other components), the adsorption constants do not possess this characteristic.

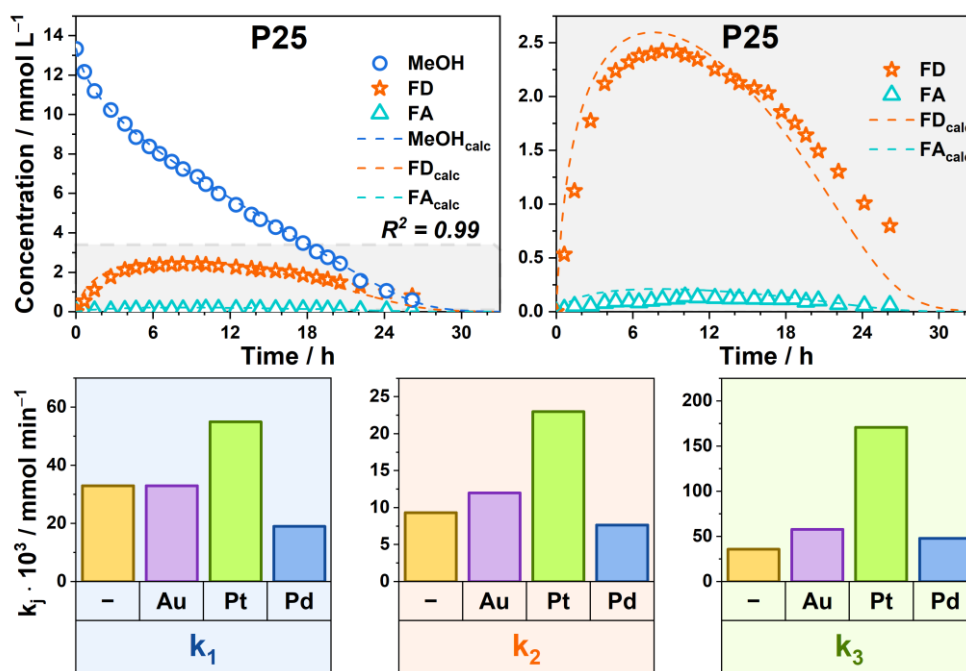


**Figure 8** Methanol oxidation data described with adsorption-based model and corresponding rate constants for methanol oxidation process:  $k_1$  –  $\text{MeOH} \rightarrow \text{FD}$ ,  $k_2$  –  $\text{FD} \rightarrow \text{FA}$ ,  $k_3$  –  $\text{FA} \rightarrow \text{CO}_2$ .

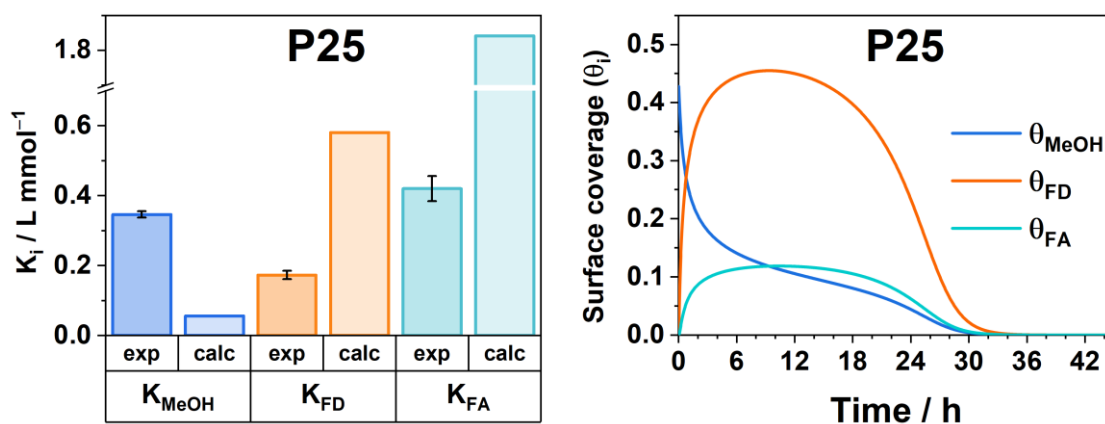


Figure 9 Adsorption equilibrium constants (left), calculated surface coverage for MeOH photocatalytic oxidation with P25 (right).

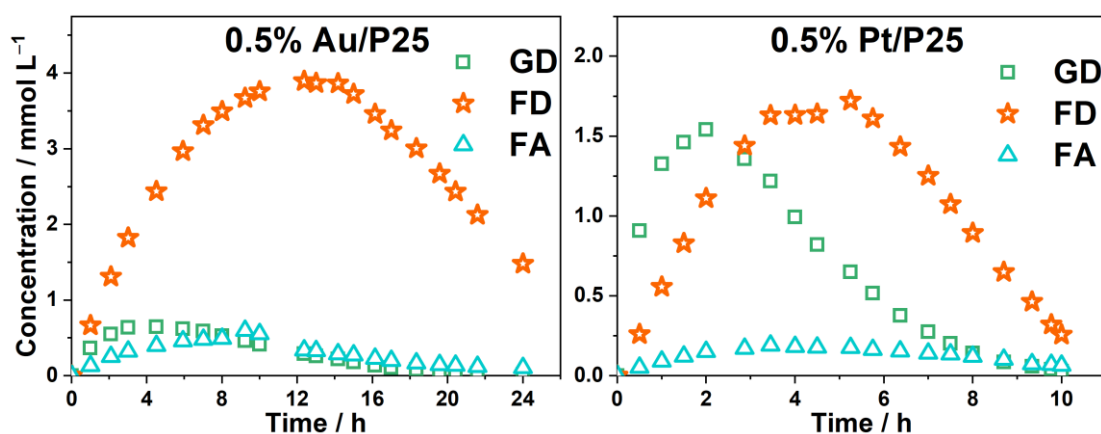


Figure 10 Ethylene glycol intermediate oxidation kinetics with 0.5% Au/P25 (left) and 0.5% Pt/P25 (right).

Figure 9 shows the values of adsorption constants for MeOH, FD, and FA, obtained experimentally (exp) and calculated via the adsorption-based model implementation (calc) for calculations of methanol oxidation on P25. For other samples, the calculated constants differ from the experimental ones in a similar manner, which is consistent with conclusion from [48] that metal deposition does not significantly alter adsorption properties.

The calculated constants for FD and FA adsorption are higher than the experimental ones, which is not the case for methanol adsorption. The decrease in the calculated constant for MeOH can be associated with its conversion to formaldehyde on the initial stage. Formaldehyde, being formed directly on the surface during the reaction (rather than adsorbed from the solution), gains an adsorption advantage over methanol and occupies a larger portion of the surface (Figure 9). The discrepancy between the calculated and experimental adsorption constants for FD and FA can also be associated with the shift in adsorption equilibrium upon their formation on the surface. The increase in these constants illustrates that they are (intermediate) reaction products.

### 3.4. Ethylene glycol oxidation pathway research and kinetic modelling

The oxidation of ethylene glycol (EG) is a complex process involving several sequential and parallel reactions [15,69]. EG oxidation can proceed via C-C bond cleavage to form

two formaldehyde (FD) molecules, which are then oxidized to formic acid (FA), and finally to carbon dioxide. An alternative pathway involves the initial oxidation of EG to glycolaldehyde (GD), which is subsequently oxidized to formaldehyde and formic acid. Although glycolic acid can be formed as EG oxidation product via electrocatalysis or photocatalysis, it was not detected in reaction mixture. This observation aligns with results reported in [20]. Consequently, glycolic acid is not included in the proposed reaction pathway. It is important to note that the accumulation of intermediate products – their formation sequence and concentrations – varies depending on the actual catalyst composition. For instance, when using 0.5% Au/P25, FD and GD are formed simultaneously (Figure 10). In contrast, oxidation with 0.5% Pt/P25 and 0.5% Pd/P25 catalysts, glycolaldehyde is primarily formed first during EG oxidation, while formaldehyde accumulation begins a bit later (Figure 10), and its yield is approximately halved. This suggests the predominance of an EG transformation pathway that avoids C-C bond cleavage.

Like the accumulation of FD observed during MeOH photocatalytic oxidation, intermediates such as FD and GD also accumulate during the EG oxidation. Meanwhile, FA concentration reaches a steady state. Based on experimental results and literature data [19,20], the following reaction scheme for photocatalytic ethylene glycol oxidation has been proposed (Figure 11).

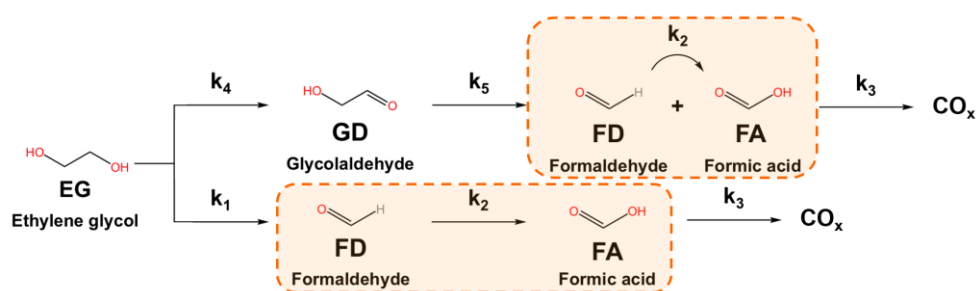


**Figure 11** Proposed scheme for photocatalytic oxidation of ethylene glycol, including main water-dissolved oxidation intermediates.

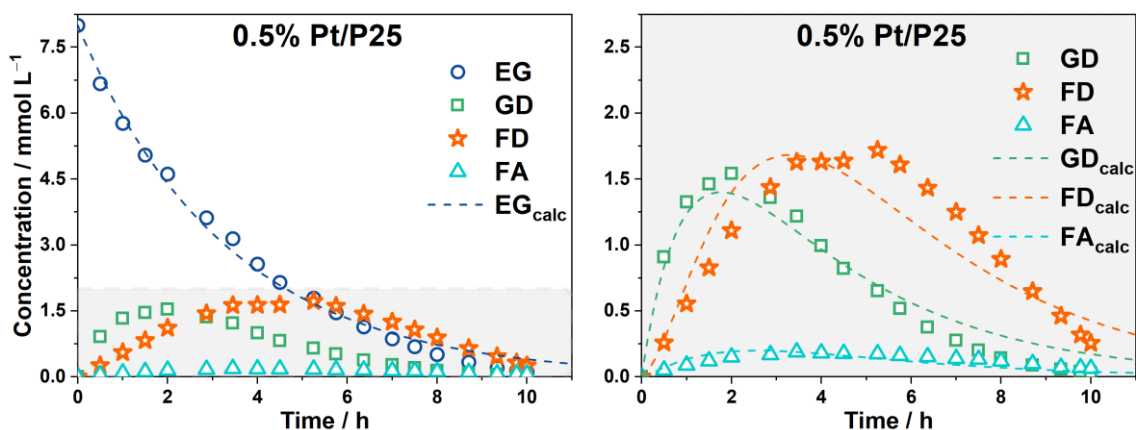


**Figure 12** Pseudo-first order kinetic model for EG photocatalytic oxidation with 0.5% Pt/P25.

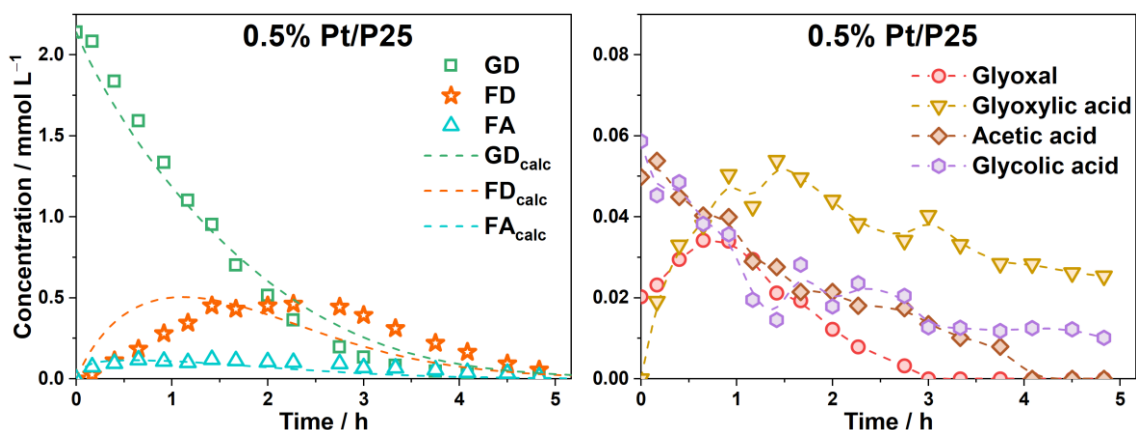


**Figure 13** Glycolaldehyde oxidation kinetics with 0.5% Pt/P25 (left) described with adsorption-based model and minor intermediate products of glycolaldehyde with 0.5% Pt/P25 (right).

The experimental kinetic curves for EG photooxidation were compared with those calculated using the pseudo-first-order model (Figure 12). As in the case of methanol oxidation, pseudo-first-order model provides a good description of the experimental data ( $R^2 = 0.98$ ) with a still noticeable difference between calculated and experimental data of the ethylene glycol concentration decrease in the middle of the process and at the final stage.

To improve the calculation results for a better fitting of experimental EG oxidation data, it is necessary to apply the adsorption-based kinetic model the same as it used for MeOH oxidation kinetics. This requires data of the GD oxidation rate constant, while the rate constant values for FD and FA oxidation are available from methanol oxidation calculations. To determine the GD oxidation rate constant value, additional experiments were carried out.

### 3.4.1. Glycolaldehyde photooxidation

Among the oxidation products of glycolaldehyde (GD), formaldehyde (FD), formic acid (FA), glyoxal, glyoxylic acid, glycolic acid, and acetic acid are detected (Figure 13). Oxidation of GD can proceed via C–C bond cleavage to form formaldehyde and formic acid. Alternatively, the following transformation pathways might occur without C–C bond cleavage: glycolaldehyde  $\rightarrow$  glyoxal  $\rightarrow$  glyoxylic acid; glycolaldehyde  $\rightarrow$  glycolic acid. Such transformations might occur in the bulk solution involving  $\cdot\text{OH}$  radicals, whereas C–C bond cleavage presumably occurs on the catalyst surface involving holes [19,20]. This could explain why minor oxidation products of glycolaldehyde are not observed during ethylene glycol oxidation: GD is formed on the surface, and although a part of it desorbs into the solution, C–C bond cleavage is the most probable pathway in this case. Glyoxal,

glycolic acid, and glyoxylic acid are further to be transformed into C1-products and CO<sub>2</sub> (Figure 14). The formation of acetic acid is likely to occur via a two-electron oxidation of acetaldehyde, potentially generated on the surface from glycolaldehyde [20].

The minor products are formed in small quantities and have negligible impact on TOC conversion. Therefore, they are not included explicitly in the kinetic modeling of glycolaldehyde oxidation and the simplified reaction scheme for calculations is GD → FD + FA (highlighted in green, Figure 14). Figure 13 shows the adsorption-based model's fit to the kinetic data for glycolaldehyde oxidation with 0.5% Pt/P25. The discrepancies between the calculations and the experimental results may be attributed to the oversimplification of the proposed reaction pathway. Despite this, the model provides a good representation of GD concentration decrease ( $R^2 = 0.97$ ).

### 3.4.2. Adsorption-based model application for ethylene glycol photooxidation

After calculation the rate constant  $k_5$  for GD transformation into FD and FA, the remaining unknown rate constants for EG conversion are  $k_1$  for EG → FD and  $k_4$  for EG → GD, along with the adsorption equilibrium constants for all components in the system:  $K_{EG}$ ,  $K_{FD}$ ,  $K_{FA}$ , and  $K_{GD}$ . When freely optimizing all parameters for different systems (0.5% M/P25, M = Au, Pt, Pd), the rate constant  $k_1$  attained negative values

(except for 0.5% Au/P25). Consequently, the EG → FD conversion step was excluded for three samples. This exclusion does not imply the total absence of this pathway (at least for some catalysts), but it reduces the number of unknown variables and simplifies calculations for these systems. Thus, the rate constant values for all EG transformation steps (Figure 15) and adsorption constants for all components were obtained.

Platinization of P25 significantly accelerates the initial EG decomposition step, with Pd and Au deposition providing less pronounced enhancement. For 0.5% Au/P25, EG decomposition predominantly proceeds through C-C bond cleavage with the formation of two FD molecules, whereas other catalysts favor EG oxidation to GD. The glycolaldehyde conversion to formaldehyde and formic acid proceeds most rapidly with pristine and platinized P25, while Pd and Au deposition reduces the rate of this step.

The agreement between experimental data and calculated kinetic curves for EG oxidation in the presence of 0.5% Pt/P25 is illustrated in Figure 16. As expected, the adsorption-based model provides a precise representation of EG oxidation kinetic data at low concentrations than the pseudo-first-order kinetic model near the ending of the conversion process ( $R^2 = 0.998$ ). Moreover, the adsorption-based model more accurately describes the behavior of intermediate products.

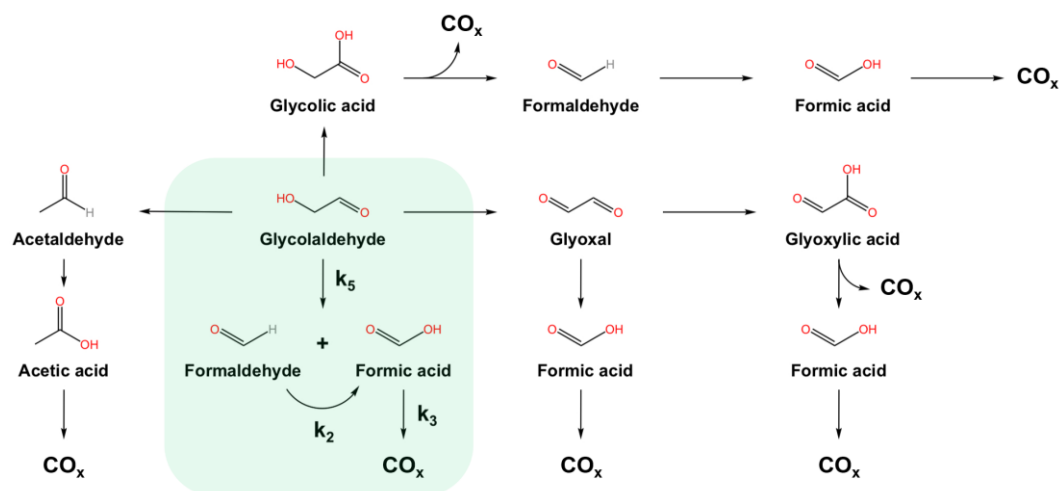


Figure 14 Proposed scheme for photocatalytic oxidation of glycolaldehyde.

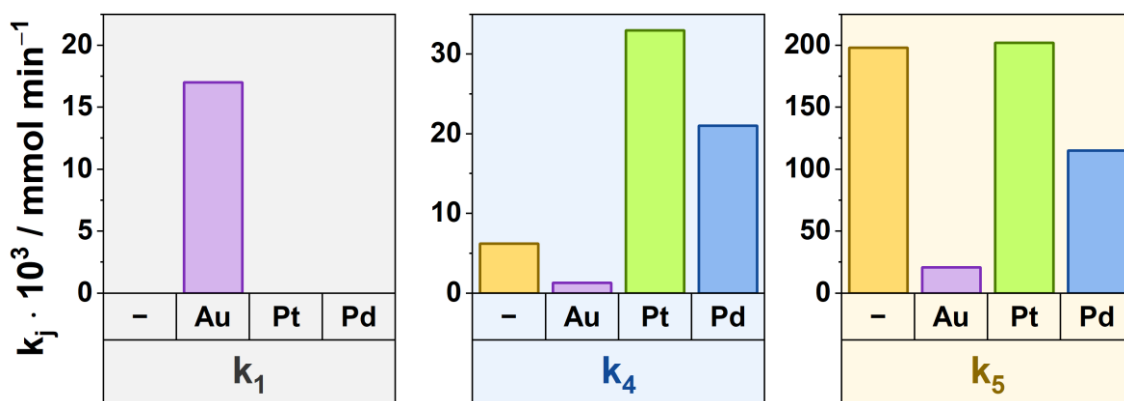


Figure 15 Rate constants for EG transformations calculated via the adsorption-based model implementation.

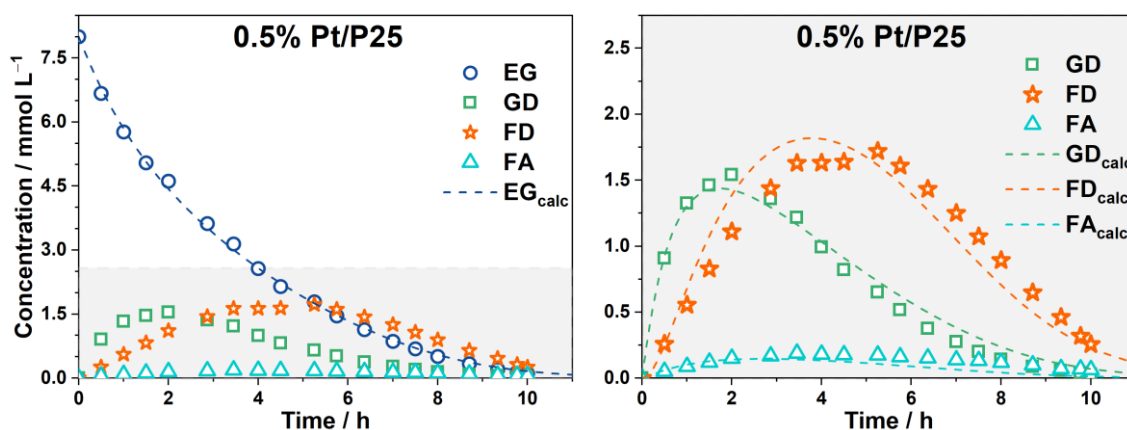


Figure 16 Ethylene glycol oxidation kinetics described with adsorption-based model for 0.5% Pt/P25.

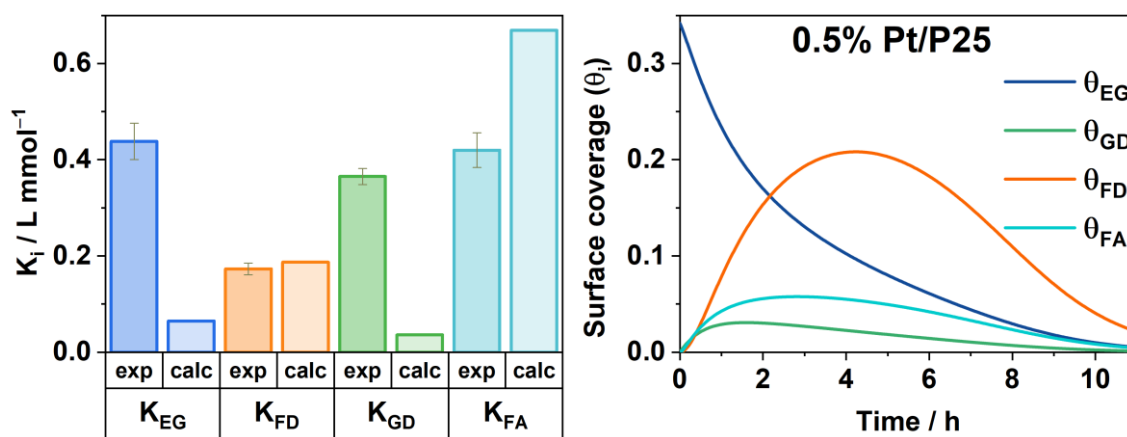


Figure 17 Adsorption equilibrium constants (left) and calculated surface coverage during methanol photocatalytic oxidation with 0.5% Pt/P25 (right).

The adsorption equilibrium constant (Figure 17) behavior follows the same trend as for methanol oxidation studies: the calculated  $K_{EG}$  is lower than experimental values due to intensive surface accumulation of oxidation intermediates FD, GD, FA. Increased calculated values for  $K_{FD}$  and  $K_{FA}$  relative to experimental data reflect again disrupted adsorption equilibrium during their surface formation. The decreased  $K_{GD}$  may stem from its high consumption rate.

#### 4. Limitations

The aim of this work was not to determine the optimal parameters of the photooxidation process for each individual catalyst. We aimed to develop and validate a kinetic modeling framework capable of describing the multi-step oxidation of model pollutants. To ensure a valid comparison, all experiments were performed under standardized conditions. A single metal loading of 0.5 wt% was selected for Pt, Pd, and Au, as it represents a mid-point within the most frequently reported range in the literature (0.1–2.0 wt%). With maintaining constant loading, the observed differences can be attributed primarily to the nature of the metal cocatalyst, rather than to variations in their dispersion and particle size.

The reaction parameters (light intensity, initial pollutant concentration, catalyst loading, oxygen flow) were fixed at values corresponding to the maximum oxidation

rate observed for the unmodified P25 reference (Figure S13). This approach ensures that any changes observed for the modified samples are attributed to their differences, and not to variations in conditions.

The implemented adsorption-based model effectively describes photocatalytic transformation kinetics while accounting for process heterogeneity. It is worth noting that the model does not currently incorporate the effects of light intensity on photooxidation kinetics, as discussed in [70,71]. Additionally, it does not account for variations in light absorption capacity, treating light intensity as a constant parameter. Both parameters can be considered when modifying the process modeling approach under consideration, which can lead to increased accuracy of calculations.

It is also important to note that while this work employs an apparent adsorption constant value, which differs from a static equilibrium constant, in a real process this constant will depend on the presence and concentration of reaction participants in the solution. This factor could contribute to a more refined model, and accounting for such a non-equilibrium parameter may improve the  $R^2$  of modeling the transformations in the studied systems. But introducing a time-dependent adsorption constant would complicate the calculation scheme and significantly increase the degree of freedom in the system.

## 5. Conclusions

In this work, we investigated M-modified TiO<sub>2</sub> P25 (M = Au, Pt, Pd), prepared by chemical reduction deposition method, in the photocatalytic oxidation of ethylene glycol and methanol in aqueous solutions. The highest degradation rates were achieved with Pt deposition: the corresponding decrease in TOC values were  $(31.0 \pm 0.5) \mu\text{mol(C) L}^{-1} \text{min}^{-1}$  for ethylene glycol and  $(24.4 \pm 2.6) \mu\text{mol(C) L}^{-1} \text{min}^{-1}$  for methanol.

The photooxidation of ethylene glycol and methanol proceeds stepwise in both cases. The intermediate transformation processes cause the nonlinear decrease in TOC at the beginning of the process. During the oxidation of organic substrates, products with aldehyde groups accumulate, and their transformation is one of the slow stages due to adsorption limitations. The apparent oxidation rate constants for formic acid are the highest, and the concentrations of formic acid in both cases reach steady-state values. The lowest observed reaction rate constant for both processes corresponds to the oxidation of formaldehyde, while the overall process is limited by the initial alcohol oxidation step.

Kinetic modeling of the photocatalytic oxidation of methanol and ethylene glycol in aqueous solutions on 0.5% M/P25 samples (where M = Au, Pt, Pd) showed that Pt nanoparticles accelerate almost all stages of the processes (except for the transformation of methanol to formaldehyde and glycolaldehyde to formaldehyde and formic acid). Pd deposition most noticeably accelerates the stage of ethylene glycol conversion to glycolaldehyde and, to a lesser extent, the stage of formic acid oxidation to final products; in other cases, Pd deposition leads to a decrease in the rate constant of the stage compared to unmodified P25. Au deposition accelerates the stages of formaldehyde oxidation to formic acid and formic acid oxidation to final products. For the sample with gold addition, ethylene glycol degradation with C–C bond cleavage is more characteristic. In contrast, the transformations of methanol to formaldehyde, glycolaldehyde to formaldehyde and formic acid, as well as ethylene glycol to glycolaldehyde are slowed down upon Au deposition.

Since photoinduced transformations occur predominantly on the photocatalyst surface, accurate kinetics modeling must account for the distribution of components between the surface and the bulk reaction mixture.

### Supplementary materials

The supplementary materials are available on the corresponding online page. **Figure S1:** Examples of HPLC chromatograms of the reaction medium; **Table S1:** Retention times of organic compounds detected in the reaction medium via HPLC; **Table S2:** Calibration coefficients for organic compounds detected in the reaction medium via HPLC; **Figure S2:** Comparison of Langmuir-Hinshelwood model (a, b) with the adsorption-based model (c, d) for the formic acid oxidation modeling; **Figure S3:** XRD data for TiO<sub>2</sub> P25 and Pt-, Au-, and Pd-modified TiO<sub>2</sub> P25; **Figure S4:** XPS data for Au-modified P25 before and after photooxidation

reaction; **Table S3:** Calculated d-spacings of XRD peaks for the synthesized samples; **Figure S5:** SEM and TEM images for titania with nanoparticles of deposited metals; **Figure S6:** Monolayer capacity variation for the formic acid oxidation; **Figure S7:** Kinetic constants for FA-to-CO<sub>2</sub> oxidation and R<sup>2</sup> dependence on different monolayer capacity values; **Figure S8:** Kinetic plots of formaldehyde calculated for different values of monolayer capacity; **Figure S9:** Kinetic plots of methanol calculated for several values of monolayer capacity; **Figure S10:** Calculated rate constants for main steps of MeOH oxidation with different values of monolayer capacity:  $k_1 - \text{MeOH} \rightarrow \text{FD}$ ,  $k_2 - \text{FD} \rightarrow \text{FA}$ ,  $k_3 - \text{FA} \rightarrow \text{CO}_2$ ; **Figure S11:** Methanol oxidation data described with pseudo-first-order model (on top) and adsorption-based model (below) for initial concentration 150 mM; **Figure S12:** Calculated rate constants for MeOH oxidation with initial concentration 150 mM:  $k_1 - \text{MeOH} \rightarrow \text{FD}$ ,  $k_2 - \text{FD} \rightarrow \text{FA}$ ,  $k_3 - \text{FA} \rightarrow \text{CO}_2$ ; **Figure S13:** TOC data for EG photocatalytic oxidation over P25. Dependence on radiation intensity (top left), O<sub>2</sub> flow rate (top right), initial EG concentration (bottom left), and catalyst loading (bottom right); **Figure S14:** Methanol oxidation kinetics using 0.5% Pt/P25 with no irradiation; **Figure S15:** Calculated rate constants for EG oxidation (pseudo-first order kinetic model):  $k_1 - \text{EG} \rightarrow \text{FD}$ ,  $k_2 - \text{FD} \rightarrow \text{FA}$ ,  $k_3 - \text{FA} \rightarrow \text{CO}_2$ ,  $k_4 - \text{EG} \rightarrow \text{GD}$ ,  $k_5 - \text{GD} \rightarrow \text{FD} + \text{FA}$ .

### Data availability statement

The data are available on request from the authors.

### Acknowledgments

The authors of the paper are grateful to Ph.D. Evtushok V.Y. for valuable advice and fruitful discussion of the results of the work.

### Author contributions

Conceptualization: M.L., D.S.  
Data curation: K.L., T.F., M.L.  
Formal Analysis: K.L., T.F.  
Funding acquisition: D.K., D.S., M.L.  
Investigation: K.L., T.F., M.L.  
Methodology: M.L., K.L.  
Project administration: M.L.  
Resources: D.K., D.S., M.L.  
Software: K.L., T.F., M.L.  
Supervision: D.K., M.L.  
Validation: T.F., D.S.  
Visualization: K.L., T.F., M.L.  
Writing – original draft: K.L.  
Writing – review & editing: T.F., M.L.

### Conflict of interest

The authors declare no conflict of interest.

### Additional information

Author IDs:

Timur Fazliev, Scopus ID [59515740100](https://orcid.org/0000-0001-5951-5740);  
Dmitry Selishchev, Scopus ID [35436247300](https://orcid.org/0000-0001-3543-6247);  
Denis Kozlov, Scopus ID [35366492500](https://orcid.org/0000-0001-3536-6492);  
Mikhail Lyulyukin, Scopus ID [36988668600](https://orcid.org/0000-0001-3698-8668).

Websites:

Boriskov Institute of Catalysis, <https://en.catalysis.ru/>;

We used DeepSeek to improve the readability and language of the manuscript. The output was extensively revised and validated by the authors.

## References

- Ahuja S. Overview: modern water purity and quality. Handbook of water purity and quality. Publisher: Elsevier; 2021. 1–18.

2. Fujishima A, Honda K. Electrochemical photolysis of water at a semiconductor electrode. *Nature*. 1972;238(5358):37-8. [doi:10.1038/238037a0](https://doi.org/10.1038/238037a0)
3. Borges ME, Sierra M, Cuevas E, García RD, Esparza P. Photocatalysis with solar energy: sunlight-responsive photocatalyst based on TiO<sub>2</sub> loaded on a natural material for wastewater treatment. *Sol Energy*. 2016;135:527-35. [doi:10.1016/j.solener.2016.06.022](https://doi.org/10.1016/j.solener.2016.06.022)
4. Almaie S, Vatanpour V, Rasoulifard MH, Koyuncu I. Volatile organic compounds (VOCs) removal by photocatalysts: a review. *Chemosphere*. 2022;306:135655. [doi:10.1016/j.chemosphere.2022.135655](https://doi.org/10.1016/j.chemosphere.2022.135655)
5. Selishchev D, Lyulyukin M, Polskikh D, Kovalevskaia K, Selishcheva S, Cherepanova S, et al. Fe-decorated Bi<sub>2</sub>WO<sub>6</sub>/TiO<sub>2</sub>-N heterostructure photocatalyst for enhanced visible light-driven degradation of organic micropollutants in air. *Sep Purif Technol*. 2026;380:135146. [doi:10.1016/j.seppur.2025.135146](https://doi.org/10.1016/j.seppur.2025.135146)
6. Mishra S, Sundaram B. A review of the photocatalysis process used for wastewater treatment. *Mater Today: Proc*. 2024;102:393-409. [doi:10.1016/j.matpr.2023.07.147](https://doi.org/10.1016/j.matpr.2023.07.147)
7. Anucha CB, Altin I, Bacaksiz E, Stathopoulos VN. Titanium dioxide (TiO<sub>2</sub>)-based photocatalyst materials activity enhancement for contaminants of emerging concern (CECs) degradation: in the light of modification strategies. *Chem Eng J Adv*. 2022;10:100262. [doi:10.1016/j.cej.2022.100262](https://doi.org/10.1016/j.cej.2022.100262)
8. Mohamadpour F, Amani AM. Photocatalytic systems: reactions, mechanism, and applications. *RSC Adv*. 2024;14(30):20609-45. [doi:10.1039/D4RA03259D](https://doi.org/10.1039/D4RA03259D)
9. McGinnis B. Degradation of ethylene glycol in photo Fenton systems. *Water Res*. 2000;34(8):2346-54. [doi:10.1016/S0043-1354\(99\)00387-5](https://doi.org/10.1016/S0043-1354(99)00387-5)
10. McGinnis BD, Adams VD, Middlebrooks EJ. Degradation of ethylene glycol using Fenton's reagent and UV. *Chemosphere*. 2001;45(1):101-8. [doi:10.1016/S0045-6535\(00\)00597-X](https://doi.org/10.1016/S0045-6535(00)00597-X)
11. Wang Y, Liu M, Miao Q, Wu P, He J, Liu C, et al. Rapid green degradation of ethylene glycol-based antifreeze wastewater via a coupled photolytic and photocatalytic double-pathway mechanism. *J Water Process Eng*. 2025;71:107191. [doi:10.1016/j.jwpe.2025.107191](https://doi.org/10.1016/j.jwpe.2025.107191)
12. Ardila-Arias AN, Berrío-Mesa E, Arriola-Villaseñor E, Álvarez-Gómez WF, Hernández-Maldonado JA, Zepeda-Partida TA, et al. Degradation of ethylene glycol through photo-Fenton heterogeneous system. *Rev Ing Univ Medellín*. 2019;18(35):91-109. [doi:10.22395/riuv.v18n35a6](https://doi.org/10.22395/riuv.v18n35a6)
13. Barash S, Covington J, Tamulonis C. Preliminary data summary airport deicing operations (Revised). Washington: United States Environmental Protection Agency; 2000. 447 p.
14. Qi K, Li Z, Zhang C, Tan X, Wan C, Liu X, et al. Biodegradation of real industrial wastewater containing ethylene glycol by using aerobic granular sludge in a continuous-flow reactor: performance and resistance mechanism. *Biochem Eng J*. 2020;161:107711. [doi:10.1016/j.bej.2020.107711](https://doi.org/10.1016/j.bej.2020.107711)
15. Fazliev T, Lyulyukin M, Kozlov D, Selishchev D. Kinetic aspects of ethylene glycol degradation using UV-C activated hydrogen peroxide (H<sub>2</sub>O<sub>2</sub>/UV-C). *Molecules*. 2024;30(1):49. [doi:10.3390/molecules30010049](https://doi.org/10.3390/molecules30010049)
16. Araña J, Méndez JAO, Melián JAH, Rodríguez JMD, Díaz OG, Peña JP. Thermal effect of carboxylic acids in the degradation by photo-Fenton of high concentrations of ethylene glycol. *Appl Catal B: Environ*. 2012;113-114:107-15. [doi:10.1016/j.apcatb.2011.11.025](https://doi.org/10.1016/j.apcatb.2011.11.025)
17. Miyazaki K, Matsumiya T, Abe T, Kurata H, Fukutsuka T, Kojima K, et al. Electrochemical oxidation of ethylene glycol on Pt-based catalysts in alkaline solutions and quantitative analysis of intermediate products. *Electrochim Acta*. 2011;56(22):7610-4. [doi:10.1016/j.electacta.2011.06.078](https://doi.org/10.1016/j.electacta.2011.06.078)
18. Chauhan NL, Juvekar VA, Sarkar A. Oxidation of ethylene glycol: unity of chemical and electrochemical catalysis. *Electrochim Sci Adv*. 2022;2(2):e2100092. [doi:10.1002/elsa.202100092](https://doi.org/10.1002/elsa.202100092)
19. Roebuck L, Daly H, Lan L, Parker J, Gostick A, Skillen N, et al. H<sub>2</sub> production from the photocatalytic reforming of ethylene glycol: effect of TiO<sub>2</sub> crystalline phase on photo-oxidation mechanism. *J Catal*. 2025;442:115876. [doi:10.1016/j.jcat.2024.115876](https://doi.org/10.1016/j.jcat.2024.115876)
20. Berto TF, Sanwald KE, Eisenreich W, Gutiérrez OY, Lercher JA. Photoreforming of ethylene glycol over Rh/TiO<sub>2</sub> and Rh/GaN:ZnO. *J Catal*. 2016;338:68-81. [doi:10.1016/j.jcat.2016.02.021](https://doi.org/10.1016/j.jcat.2016.02.021)
21. Klauson D, Preis S. The influence of iron ions on the aqueous photocatalytic oxidation of deicing agents. *Int J Photoenergy*. 2007;2007:089359. [doi:10.1155/2007/89359](https://doi.org/10.1155/2007/89359)
22. Kim KN, Hoffmann MR. Heterogeneous photocatalytic degradation of ethylene glycol and propylene glycol. *Korean J Chem Eng*. 2008;25(1):89-94. [doi:10.1007/s11814-008-0015-4](https://doi.org/10.1007/s11814-008-0015-4)
23. Zhang J, Nosaka Y. Photocatalytic oxidation mechanism of methanol and the other reactants in irradiated TiO<sub>2</sub> aqueous suspension investigated by OH radical detection. *Appl Catal B: Environ*. 2015;166-167:32-6. [doi:10.1016/j.apcatb.2014.11.006](https://doi.org/10.1016/j.apcatb.2014.11.006)
24. Xiao M, Baktash A, Lyu M, Zhao G, Jin Y, Wang L. Unveiling the role of water in heterogeneous photocatalysis of methanol conversion for efficient hydrogen production. *Angew Chem Int Ed*. 2024;63(18):e202402004. [doi:10.1002/anie.202402004](https://doi.org/10.1002/anie.202402004)
25. Chiarello GL, Aguirre MH, Selli E. Hydrogen production by photocatalytic steam reforming of methanol on noble metal-modified TiO<sub>2</sub>. *J Catal*. 2010;273(2):182-90. [doi:10.1016/j.jcat.2010.05.012](https://doi.org/10.1016/j.jcat.2010.05.012)
26. Augustin A, Ganguly P, Shenoy S, Chuaicham C, Pillai SC, Sasaki K, et al. Impact of hole scavengers on efficient photocatalytic hydrogen production. *Adv Sustainable Syst*. 2024;8(10):2400321. [doi:10.1002/adsu.202400321](https://doi.org/10.1002/adsu.202400321)
27. Denisov N, Yoo J, Schmuki P. Effect of different hole scavengers on the photoelectrochemical properties and photocatalytic hydrogen evolution performance of pristine and Pt-decorated TiO<sub>2</sub> nanotubes. *Electrochim Acta*. 2019;319:61-71. [doi:10.1016/j.electacta.2019.06.173](https://doi.org/10.1016/j.electacta.2019.06.173)
28. Yilmaz B, Ünal U. Photoelectrochemical investigation of hole scavengers for photocatalytic hydrogen evolution reaction on perovskite-type niobate nanosheets. *ChemPhotoChem*. 2025;9(1):e202400297. [doi:10.1002/cptc.202400297](https://doi.org/10.1002/cptc.202400297)
29. García-López EI, Palmisano L, Marci G. Overview on photoreforming of biomass aqueous solutions to generate H<sub>2</sub> in the presence of g-C<sub>3</sub>N<sub>4</sub>-based materials. *ChemEngineering*. 2023;7(1):11. [doi:10.3390/chemengineering7010011](https://doi.org/10.3390/chemengineering7010011)
30. Ismail AA, Robben L, Bahnmann DW. Study of the efficiency of UV and visible-light photocatalytic oxidation of methanol on mesoporous RuO<sub>2</sub>-TiO<sub>2</sub> nanocomposites. *ChemPhysChem*. 2011;12(5):982-91. [doi:10.1002/cphc.201000936](https://doi.org/10.1002/cphc.201000936)
31. Wei Z, Ji Y, Bielan Z, Yue X, Xu Y, Sun J, et al. Platinum-modified rod-like titania mesocrystals with enhanced photocatalytic activity. *Catalysts*. 2024;14(4):283. [doi:10.3390/catal14040283](https://doi.org/10.3390/catal14040283)
32. Li X, Wei H, Song T, Lu H, Wang X. A review of the photocatalytic degradation of organic pollutants in water by modified TiO<sub>2</sub>. *Water Sci Technol*. 2023;88(6):1495-507. [doi:10.2166/wst.2023.288](https://doi.org/10.2166/wst.2023.288)
33. Armaković SJ, Savanović MM, Armaković S. Titanium dioxide as the most used photocatalyst for water purification: an overview. *Catalysts*. 2022;13(1):26. [doi:10.3390/catal13010026](https://doi.org/10.3390/catal13010026)
34. Bahnmann DW, Hilgendorff M, Memming R. Charge carrier dynamics at TiO<sub>2</sub> particles: reactivity of free and trapped holes. *J Phys Chem B*. 1997;101(21):4265-75. [doi:10.1021/jp9639915](https://doi.org/10.1021/jp9639915)
35. Ollis D. Kinetic analysis of liquid phase photocatalysis and photolysis: a frequent disguise! *Catal Today*. 2020;340:7-11. [doi:10.1016/j.cattod.2018.11.011](https://doi.org/10.1016/j.cattod.2018.11.011)
36. Chakravorty A, Roy S. A review of photocatalysis, basic principles, processes, and materials. *Sustainable Chem Environ*. 2024;8:100155. [doi:10.1016/j.scenv.2024.100155](https://doi.org/10.1016/j.scenv.2024.100155)

37. Amano F, Yamamoto A, Kumagai J. Highly active rutile TiO<sub>2</sub> for photocatalysis under violet light irradiation at 405 nm. *Catalysts*. 2022;12(10):1079. doi:10.3390/catal12101079
38. Eddy DR, Permana MD, Sakti LK, Sheha GAN, Solihudin, Hidayat S, et al. Heterophase polymorph of TiO<sub>2</sub> (anatase, rutile, brookite, TiO<sub>2</sub> (B)) for efficient photocatalyst: fabrication and activity. *Nanomaterials*. 2023;13(4):704. doi:10.3390/nano13040704
39. Fazliev T, Polskikh D, Selishchev D. Photocatalytic production of H<sub>2</sub>O<sub>2</sub> over rutile TiO<sub>2</sub> supported with Pd nanoparticles. *Appl Surf Sci*. 2025;686:162124. doi:10.1016/j.apsusc.2024.162124
40. Žerjav G, Žižek K, Zavašnik J, Pintar A. Brookite vs. rutile vs. anatase: what's behind their various photocatalytic activities? *J Environ Chem Eng*. 2022;10(3):107722. doi:10.1016/j.jece.2022.107722
41. Ding L, Yang S, Liang Z, Qian X, Chen X, Cui H, et al. TiO<sub>2</sub> nanobelts with anatase/rutile heterophase junctions for highly efficient photocatalytic overall water splitting. *J Colloid Interface Sci*. 2020;567:181–9. doi:10.1016/j.jcis.2020.02.014
42. Hernández-Laverde M, Murcia JJ, Morante N, Sannino D, Vaiano V, Navio JA, et al. Photocatalytic activity enhancement by noble metal deposition on faceted F-TiO<sub>2</sub> synthesised by microwave assisted method. A study of selective oxidation of gas-phase ethanol in a FBPR reactor. *Catal Today*. 2024;433:114645. doi:10.1016/j.cattod.2024.114645
43. Sakthivel S, Shankar MV, Palanichamy M, Arabindoo B, Bahnemann DW, Murugesan V. Enhancement of photocatalytic activity by metal deposition: characterisation and photonic efficiency of Pt, Au and Pd deposited on TiO<sub>2</sub> catalyst. *Water Res*. 2004;38(14–15):3001–8. doi:10.1016/j.watres.2004.04.046
44. Sescu AM, Favier L, Lutic D, Soto-Donoso N, Ciobanu G, Harja M. TiO<sub>2</sub> doped with noble metals as an efficient solution for the photodegradation of hazardous organic water pollutants at ambient conditions. *Water*. 2020;13(1):19. doi:10.3390/w13010019
45. Wang K, Wei Z, Ohtani B, Kowalska E. Interparticle electron transfer in methanol dehydrogenation on platinum-loaded titania particles prepared from P25. *Catal Today*. 2018;303:327–33. doi:10.1016/j.cattod.2017.08.046
46. Lakshmanareddy N, Rao VN, Cheralathan KK, Subramaniam EP, Shankar MV. Pt/TiO<sub>2</sub> nanotube photocatalyst – effect of synthesis methods on valance state of Pt and its influence on hydrogen production and dye degradation. *J Colloid Interface Sci*. 2019;538:83–98. doi:10.1016/j.jcis.2018.11.077
47. Wang K, Kowalska E. Property-governed performance of platinum-modified titania photocatalysts. *Front Chem*. 2022;10:972494. doi:10.3389/fchem.2022.972494
48. Jin X, Li C, Xu C, Guan D, Cheruvathur A, Wang Y, et al. Photocatalytic C–C bond cleavage in ethylene glycol on TiO<sub>2</sub>: a molecular level picture and the effect of metal nanoparticles. *J Catal*. 2017;354:37–45. doi:10.1016/j.jcat.2017.08.004
49. Michaelson HB. The work function of the elements and its periodicity. *J Appl Phys*. 1977;48(11):4729–33. doi:10.1063/1.323539
50. Kong J, Jiang C, Rui Z, Liu S, Xian F, Ji W, et al. Photothermocatalytic synergistic oxidation: an effective way to overcome the negative water effect on supported noble metal catalysts for VOCs oxidation. *Chem Eng J*. 2020;397:125485. doi:10.1016/j.cej.2020.125485
51. Chen J, Ollis DF, Rulkens WH, Bruning H. Photocatalyzed oxidation of alcohols and organochlorides in the presence of native TiO<sub>2</sub> and metallized TiO<sub>2</sub> suspensions. Part (I): photocatalytic activity and pH influence. *Water Res*. 1999;33(3):661–8. doi:10.1016/S0043-1354(98)00261-9
52. Lyulyukin M, Kovalevskiy N, Prosvirin I, Selishchev D, Kozlov D. Thermo-photoactivity of pristine and modified titania photocatalysts under UV and blue light. *J Photochem Photobiol A: Chem*. 2022;425:113675. doi:10.1016/j.jphotochem.2021.113675
53. Makuła P, Pacia M, Macyk W. How to correctly determine the band gap energy of modified semiconductor photocatalysts based on UV–Vis spectra. *J Phys Chem Lett*. 2018;9(23):6814–7. doi:10.1021/acs.jpcclett.8bo2892
54. Landi S, Segundo IR, Freitas E, Vasilevskiy M, Carneiro J, Tavares CJ. Use and misuse of the Kubelka-Munk function to obtain the band gap energy from diffuse reflectance measurements. *Solid State Commun*. 2022;341:114573. doi:10.1016/j.ssc.2021.114573
55. Tran HD, Nguyen DQ, Do PT, Tran UNP. Kinetics of photocatalytic degradation of organic compounds: a mini-review and new approach. *RSC Adv*. 2023;13(24):16915–25. doi:10.1039/D3RA01970E
56. Rytwo G, Zelkind AL. Evaluation of kinetic pseudo-order in the photocatalytic degradation of ofloxacin. *Catalysts*. 2021;12(1):24. doi:10.3390/catal12010024
57. Jawad AH, Mubarak NSA, Ishak MAM, Ismail K, Nawawi WI. Kinetics of photocatalytic decolorization of cationic dye using porous TiO<sub>2</sub> film. *J Taibah Univ Sci*. 2016;10(3):352–62. doi:10.1016/j.jtusci.2015.03.007
58. Korobov VI, Ochkov VF. Chemical kinetics with Mathcad and Maple. Springer-Verlag/Wien; 2011. 344p.
59. Nomikos GN, Panagiotopoulou P, Kondarides DI, Vverykios XE. Kinetic and mechanistic study of the photocatalytic reforming of methanol over Pt/TiO<sub>2</sub> catalyst. *Appl Catal B: Environ*. 2014;146:249–57. doi:10.1016/j.apcatb.2013.03.018
60. Childs L. Is photocatalysis catalytic? *J Catal*. 1980;66(2):383–90. doi:10.1016/0021-9517(80)90041-X
61. Qu T, Yao X, Owens G, Gao L, Zhang H. A sustainable natural clam shell derived photocatalyst for the effective adsorption and photodegradation of organic dyes. *Sci Rep*. 2022;12:2988. doi:10.1038/s41598-022-06981-3
62. Rioja N, Zorita S, Peñas FJ. Effect of water matrix on photocatalytic degradation and general kinetic modeling. *Appl Catal B: Environ*. 2016;180:330–5. doi:10.1016/j.apcatb.2015.06.038
63. Lin Y-C, Chen C-H, Chen K-S, Peng Y-P, Lin Y-C, Huang S-W, et al. Green synthesized palladium coated titanium nanotube arrays for simultaneous azo-dye degradation and hydrogen production. *Catalysts*. 2020;10(11):1330. doi:10.3390/catal10111330
64. Nasrollahzadeh M, Shafiei N, Eslamipannah M, Fakhri P, Jaleh B, Orooji Y, et al. Preparation of Au nanoparticles by Q switched laser ablation and their application in 4-nitrophenol reduction. *Clean Techn Environ Policy*. 2020;22:1715–24. doi:10.1007/s10098-020-01899-8
65. Pramanik G, Humpolickova J, Valenta J, Kundu P, Bals S, Bour P, et al. Gold nanoclusters with bright near-infrared photoluminescence. *Nanoscale*. 2018;10:3792–8. doi:10.1039/C7NR06050E
66. Kozlova EA, Lyubina TP, Nasalevich MA, Vorontsov AV, Miller AV, Kaichev VV, et al. Influence of the method of platinum deposition on activity and stability of Pt/TiO<sub>2</sub> photocatalysts in the photocatalytic oxidation of dimethyl methylphosphonate. *Catal Commun*. 2011;12:597–601. doi:10.1016/j.cattcom.2010.12.007
67. Lee J, Choi W. Photocatalytic reactivity of surface platinumized TiO<sub>2</sub>: substrate specificity and the effect of Pt oxidation state. *J Phys Chem B*. 2005;109:7399–406. doi:10.1021/jp044425
68. Ollis DF. Kinetics of photocatalyzed reactions: five lessons learned. *Front Chem*. 2018;6:378. doi:10.3389/fchem.2018.00378
69. Fazliev T, Lyulyukin M, Yakhvarov D, Sinyashin O, Yakovlev V, Kozlov D, et al. Degradation, boosted with Fe<sup>2+</sup> ions, of ethylene glycol in oxygen-saturated aqueous solutions using the H<sub>2</sub>O<sub>2</sub>/UV-C oxidation system: a kinetic study. *Chimica Techno Acta*. 2025;12. doi:10.15826/chimtech.9192
70. Megatiff L, Dillert R, Bahnemann DW. Reaction rate study of the photocatalytic degradation of dichloroacetic acid in a black body reactor. *Catalysts*. 2019;9(8):635. doi:10.3390/catal9080635
71. Bloh JZ. A holistic approach to model the kinetics of photocatalytic reactions. *Front Chem*. 2019;7:128. doi:10.3389/fchem.2019.00128